# FEASIBILITY OF DETERMINING RADIOACTIVITY IN LUNGS USING A THYROID UPTAKE COUNTER

A Thesis
Presented to
The Academic Faculty

by

Ryan A. Lorio

In Partial Fulfillment
of the Requirements for the Degree
Master of Science in the
George W. Woodruff School of Mechanical Engineering

Georgia Institute of Technology
December 2005

**FEASIBILITY OF DETERMINING RADIOACTIVITY IN LUNGS USING A THYROID UPTAKE COUNTER**

Approved by:

Dr. Nolan E. Hertel, Advisor
Nuclear and Radiological Engineering
*Georgia Institute of Technology*

Dr. C.-K. Chris Wang
Nuclear and Radiological Engineering
*Georgia Institute of Technology*

Dr. Armin J. Ansari
Centers for Disease Control and Prevention

Date Approved: August 10, 2005

## ACKNOWLEDGEMENTS

One of the most basic principles I have learned is that without God, nothing is possible. He has been with me every step of the way and will continue to guide me in my future endeavors. I am extremely grateful to my family, especially my mother and father, for their continued support emotionally, spiritually, and financially. You have given more of yourselves than anyone could possibly ask. You are my true inspirations and I love you all very much.

As for the technical community, I would first like to thank my advisor, Dr. Nolan Hertel, for his academic, social, and always lighthearted guidance. Your contribution to my education and future success will never be forgotten. Next, I would like to thank my thesis committee, Dr. Chris Wang and Dr. Armin Ansari, for taking the time to review my research and for providing me with helpful insights and recommendations. I am also very grateful to my counterparts at the CDC, SC&A, Inc. and Hershey Medical Center for their support in obtaining and relaying their measurement data and to Jim Hardeman of the Georgia Department of Natural Resources for his recommendations in this work.

I would also like to thank those students who have helped me to formulate and develop my thesis, especially Zhonglu Wang, Jesson Hutchinson, and Ashley Manzoor. I would also like to extend a special thanks to Dwayne Blaylock and Eric Burgett who were my MCNP support desk, helping with all of my computer needs.

Finally, I would like to thank Virginia Maniquis for simply being herself. Never have I met a more compassionate, selfless, and all around beautiful person. I am truly blessed to have you in my life. Thank you all very much.

## TABLE OF CONTENTS

## LIST OF TABLES

## LIST OF FIGURES

## SUMMARY

In the event of a radiological attack on a civilian population, there will be a need to screen a large number of people for contamination in a timely and effective manner. With the increasing presence of nuclear medicine departments in local hospitals, a variety of radiation detection and imaging systems will exist that could be used to evaluate incoming patients. Utilizing the Monte Carlo N-Particle radiation transport code version 5 (MCNP5), developed by Los Alamos National Laboratory, the feasibility of using a thyroid uptake counter for detecting lung contamination has been investigated.

A variety of MCNP models were first created to validate the detector model and code simulations against measured data obtained from a preliminary study. Measurements were previously made by S. Cohen & Associates, Inc. (SC&A) with discrete, encapsulated sources of $^{60}$Co, $^{137}$Cs, $^{192}$Ir and $^{241}$Am in an acrylic slab phantom and in air, with the source and detector system placed various distances apart. An additional setup was used to measure the count rates from a $^{131}$I source uniformly distributed in a water-filled phantom.

The comparison of the MCNP simulations with the measurements provided the validation required to perform calculations with the code for source and detector geometries beyond those for which measurements are available. Anthropomorphic phantoms of various ages, sexes, and body masses were modeled to simulate variations in radioactive material distributions in the lungs as well as the change in detection efficiency due to the varying thicknesses of intervening tissue. The minimum detectable activity was calculated for each setup and retention fractions were used to establish the

amount of material expected to remain in the body shortly after intake. Dose correlations were used to quantify the energy that would be deposited by the inhaled radioactive material and both collimated and uncollimated detector geometries were analyzed to fully examine the detector's capabilities.

# CHAPTER 1

# INTRODUCTION

In a recent survey of some of the nation's leading experts, the probability of an attack from a weapon of mass destruction (WMD) is as high as 50 percent over the next five years with the most significant risk of attack expected to come from a radiological dispersal device (RDD) (Lugar, 2005). These devices may be implemented in a number of different forms, each having the ability to spread radioactive isotopes over a large area. If an RDD event were to take place in a metropolitan area, the result would be a large number of people ingesting or inhaling radioactive material.

Some of these materials may ultimately concentrate in various organs of the body or be distributed uniformly through the entire body over time. However, for at least a brief period after inhalation, a portion of the radioactive material will be concentrated in the lungs until cleared by the respiratory tract or absorbed into the bloodstream (Jarret et al., 2003). The ability to screen large numbers of people who may be internally contaminated with radioactive materials will be necessary so that medical intervention can be employed if needed.

The device typically used to monitor internal radioactivity in a person is known as a whole-body counter (WBC) and can be found at most large nuclear facilities. This system employs a radiation detector or a set of detectors outside of the body to measure radiations emitted by the materials deposited inside the body. The energy distributions of the measured radiation can also be used to assist in identifying the material present as well as assist in quantifying it. WBCs, however, are not readily available in metropolitan

areas because most nuclear facilities where internal contamination is of concern are somewhat removed from large population centers.

SC&A, Inc. has undertaken an evaluation for the Centers for Disease Control and Prevention (CDC) to analyze the use of more readily available radiation detection systems, such as those used in nuclear medicine procedures, to perform whole-body counting after RDD events (Anigstein et al., 2005). These systems, although not optimized for whole-body counting, are still potentially useful in determining even low body burdens of radioactive material; at least low enough to assess victims for triage. Of particular interest are those detection systems found in nuclear medicine departments at most hospitals. These instruments include nuclear medicine cameras and thyroid uptake probes. A variety of other systems that are used for assaying hospital waste streams and surveying for radioactive contamination are also being considered in the SC&A study. These systems detect radiation external to the body from radioactive materials deposited in the body by utilizing effective scanning procedures.

This thesis extends the work performed by SC&A for the use of a thyroid uptake system for monitoring lung contamination. Most of their measurements used point sources of radiation to represent material inhaled from RDD events when in actuality the radioactivity is not likely to be concentrated in a single location. Another aspect of their study simulated the distributed loadings of a radioactive source in a lung by dissolving a radioactive substance in a water phantom. Although this source distribution is more representative of an expected inhalation model, it uses a different density composition than lung, tissue, and bone and greatly simplifies the geometry of a human torso.

To exhaustively study the performance of this detection system by a measurement program would be very time intensive and costly. Instead, through the use of the highly validated MCNP Monte Carlo radiation transport code, simulations were carried out to address the response of the thyroid uptake counter to diffuse sources in human phantoms and the variation of the minimum detectable activity (MDA) levels in the lungs as a function of intervening tissue thickness. Models were also developed to include variations in the detector geometry using both collimated and uncollimated systems.

# CHAPTER 2

# BACKGROUND

There are a variety of systems and methods that are specifically designed for the detection of internally deposited radioactivity. After an RDD event, the availability and access to these technologies will be limited but an understanding of these detection systems for internal counting and their relationship to other detection systems is of value. In this section, some general aspects of internal contamination assessment and gamma-ray interactions important to spectroscopy and detection are discussed.

## 2.1 Internal Contamination Assessment

The methods for quantifying the amount of radioactivity present in an individual may be divided into two categories, namely *in vitro* and *in vivo* bioassays. For *in vitro* bioassay, the radioactivity of material excreted from the body is measured and compared to the expected intake of radioactivity for the person in consideration. The remaining activity in the body can then be estimated from this information and knowledge of the metabolism of the material in the human body. The *in vivo* method utilizes external counting equipment, such as WBCs, to detect photon radiations that are directly emitted from the body. The amount of radioactive material present can then be inferred from the knowledge of the source material, the migration of the radionuclide in the body, the physical detector placement, and the characteristics of the detection system. In an RDD event involving the public, a timely response is of the utmost concern. Therefore, the *in vivo* bioassay method will be the most effective in triaging victims for internal contamination of high enough levels to be of concern.

As mentioned previously, the only radionuclides of importance to external detection are those that emit photons (x-rays, $\gamma$-rays or bremsstrahlung radiation) or beta particles of sufficient energy to penetrate the layers of tissue typical of the human body. Once these particles escape the surface, there are a variety of whole-body or specific-organ counters that are commonly used in radiation protection and nuclear medicine that can determine the quantity and location of radioactive material in the body. WBC systems have routinely been used to monitor individuals who are commonly exposed to unsealed radioactive sources in the workplace. These systems can also be used to determine previous intakes of radionuclides using metabolic models that describe the behavior of the substance in the body. Similar techniques are used in some diagnostic medical procedures as well; an example is the thyroid probe which is used to measure the uptake of radioactive iodine in the treatment of hyperthyroidism.

These instruments and procedures have greatly improved over the years. The first measurements of radionuclides deposited in the body were performed on the radium dial painters in the mid-to-late 1920s. It was common during this period for the workers to lick the tips of their paint brushes, resulting in the ingestion of small amounts of radium each time. Schlundt and his associates were able to make rudimentary measurements regarding the amount of internally deposited radium by utilizing an electroscope positioned along the spine of a contaminated patient (Schlundt et al., 1929). In addition to performing such basic measurements, these early researchers developed techniques that could be used when monitoring internal radioactivity to provide a standard for future studies (Flinn, 1929), many of which are applicable to today's detection systems.

Once nuclear research spread to military and civilian sectors, the desire to limit internal radiation exposure to workers became a greater concern and led to the development of detection systems and techniques for that purpose. Prior to the mid-1950s, it was common to find that "*in vitro* bioassay was the only method available to assess occupational intakes of radionuclides in defense facilities" (Taylor, 2000). However, shortly thereafter, the continued development of solid scintillation and semiconductor detectors enabled the detection of radioactive emissions from areas of the body not previously covered in external bioassay techniques.

One of the most notable developments was the thallium-activated sodium iodide (NaI[Tl]) crystal. The high light yield produced in this material by ionizing radiation and the ability to shape these crystals into detectors of large diameter gave them an advantage in $\gamma$-ray detection efficiency over other systems. A variety of WBCs began to employ this technology in facilities that utilized both chair and flat-bed setups to monitor contaminated subjects. In addition, heavily shielded rooms were implemented to reduce the effect of background radiation on the number of counts registered by the detection systems (Taylor, 2000).

Thin sodium iodide crystals were also being implemented in low energy photon detection, but problems resulting from the fragility of the crystal and their high cost led to the development of other detectors for chest counting. One such development was the Phoswich detector, a thin NaI crystal sandwiched with a cesium iodide (CsI) crystal, that can be used to measure both high and low energy photons (Hickman, 1994). Further advances were made in *in vivo* counting with the development of high purity germanium

(HPGe) detectors. This detection system is known for its increased energy resolution and, therefore, the ability to distinguish between $\gamma$-rays of similar energy.

In general, however, the ability of all of these detection systems to assay radioactivity *in vivo* has been extensively analyzed and well documented. The minimum detectable activities (MDAs) attainable by these counting systems can be measured to less than one thousandth of the annual dose limit allowable for radiation workers. Even smaller amounts of radioactivity can be determined if the material is known to be concentrated in specific areas, with values being measured as low as 3 pCi (Toohey et al., 1991).

Detection at such a high level of sensitivity, however, would not be warranted in screening individuals following an RDD scenario, as indicated by the incident that occurred in Goiânia, Brazil in 1987. It was in this town that an abandoned medical source containing 1375 Ci of $^{137}$Cs was breached, contaminating people directly and indirectly to internal levels that ranged from below the MDA of the WBC system utilized (197 nCi) up to 1.6 mCi. Normal WBC facilities were not used due to their distance from the accident or because the *in vivo* activities were too high for the instrumentation (Oliveira et al., 1991). Fortunately, only a relatively small number of people were affected by this incident, but lessons from this experience and an understanding of various *in vivo* detection capabilities are useful to those confronted with a similar situation in the future.

## 2.2 Gamma-Ray Interactions

A variety of interaction possibilities exist as gamma rays pass through matter, but the most important to spectroscopy are photoelectric absorption, Compton scattering, and

pair production (Knoll, 2000). In each of these processes, it should be realized that the photon is uncharged and consequently does not cause direct ionization in the material in which it is being transported. The detection of $\gamma$-rays is dependent upon the loss of kinetic energy to electrons through scattering or complete absorption in the detection material.

The most likely interaction in which a $\gamma$-ray will deposit all of its energy to the surrounding medium is the photoelectric effect and is the predominate reaction with low energy gamma rays. In this process, the incident photon interacts with a bound inner shell electron which is then ejected from the atom (Figure 2.1). The energy of this particle is equal to that of the incident photon minus the binding energy of the photoelectron's original shell. The subsequent de-excitation of the atom results in the

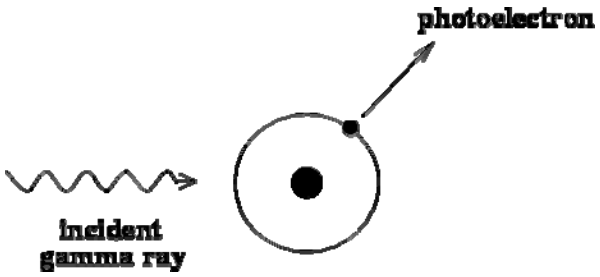


Figure 2.1: Photoelectric Absorption

emission of x-ray photons and/or Auger electrons which are stopped in a short distance within the material in comparison to the mean free path of the $\gamma$-rays (Arqueros et al., 2003).

The Compton scattering interaction, however, is a purely kinematic collision between a gamma photon and a loosely bound electron in the absorbing material. This

process dominates in the energy region of a few keV up to several MeV and unlike photoelectric absorption, only a part of the $\gamma$-ray energy is imparted to the electron (Figure 2.2).

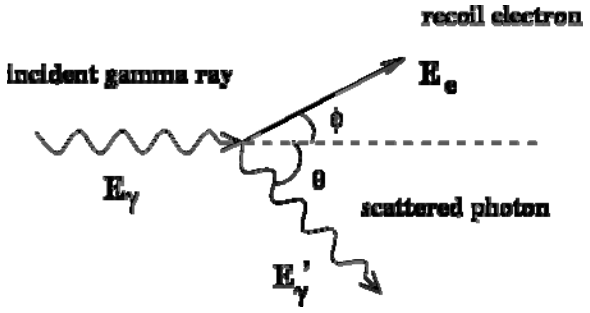


Figure 2.2: Compton Scattering

Solving the energy and momentum equations for this type of collision can yield the energy of the recoiling electron as well as the energy of the scattered photon:

$$E_e = E_\gamma - E_{\gamma'} \qquad [2.1]$$

$$E_{\gamma'} = \frac{E_\gamma}{1+(E_\gamma/m_o c^2)(1-\cos\theta)} \qquad [2.2]$$

When the scattering angle is 180º, the $\gamma$-ray is scattered backwards and the maximum energy is imparted to the electron. Even at this value, however, the energy of the electron is still less than the incident gamma. This indicates that for any scattering angle the amount of $\gamma$-ray energy absorbed by the detector in a Compton collision will be less than that of the incident photon.

The third significant interaction to gamma spectroscopy is pair production, a process that can only be achieved at energies greater than 1.022 MeV, but is only significant for incident energies of several MeV (Keenan, 1999). The reason for this energy requirement is that in this interaction, the incident $\gamma$-ray is converted into an electron-positron pair each with a rest mass of 0.511 MeV.

The positron emitted in this interaction is not a stable particle and once its kinetic energy is reduced to that of the surrounding material, will annihilate or combine with a normal electron in the absorbing medium (Knoll, 2000). This process yields two annihilation photons of equal energy as illustrated in Figure 2.3.

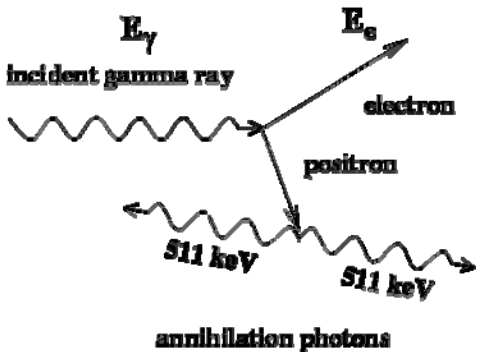


Figure 2.3: Pair Production

# CHAPTER 3

# METHODOLOGY

Monte Carlo methods have previously been used to simulate *in vivo* measurements of radionuclides. In particular, a variety of research has documented the use of Los Alamos's MCNP code to perform WBC calibrations, various phantom measurements, and simulations for targeted radiotherapy (Kramer et al., 2002; Franck et al., 2003; Autret et al., 2005). To evaluate the capabilities of a thyroid probe in assaying lung contamination, photon transport essential to radiation detection was simulated using MCNP5. A set of MCNP models was first used to validate the detector performance against previously reported results before extending the code to source-detector geometries and configurations not available in the measurement program. A summary of these simulations is detailed below and the section is concluded with an MDA formulation and an evaluation of dose coefficients applicable to these models.

## 3.1 Detection System Overview

There are a variety of thyroid uptake systems used in nuclear medicine departments across the country, but each of these systems utilizes similar detection equipment. The Atomlab 950[1] is an example of one such system and was used in SC&A's evaluation of hospital detectors as potential internal contamination monitors (Anigstein et al., 2005). This system was originally designed for thyroid uptake studies, wipe tests, and hematology tests, but a thyroid counter has been previously cited as being

[1] Biodex Medical Systems, Inc. 20 Ramsay Road, Shirley, New York 11967

"useful as an emergency whole-body counter for larger gamma exposures" (NCRP, 1980).

This particular system is based on a 2" x 2" (5 cm x 5 cm) NaI(Tl) detector coupled to a 1024-channel multi-channel analyzer. A cylindrical lead housing attached to a control arm contains the NaI crystal and photomultiplier tube. The housing also contains a cone-shaped lead collimator that extends 15.2 cm from the face of the detector towards the subject to be assayed and has an aperture of approximately 9.2 cm. Based on these dimensions and the material compositions, a MCNP model of the detector was created and has been utilized in a variety of scenarios (Figure 3.1).

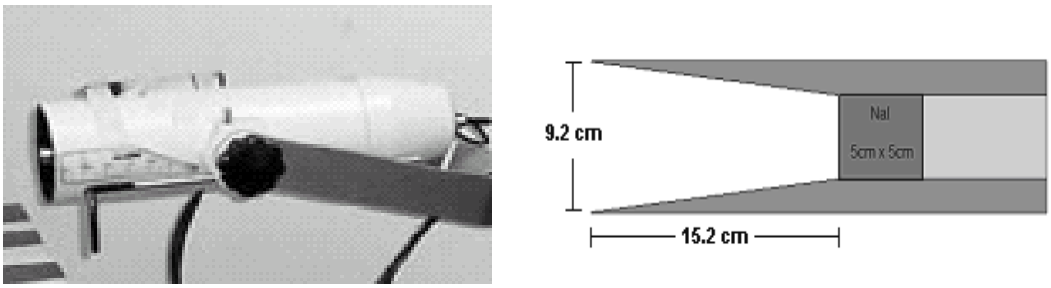


Figure 3.1: Atomlab 950 (Anigstein et al., 2005) and MCNP 2-D Visualization

The radioisotopes investigated in this work are of those 80 cited as being of the highest security concern and the most likely to be used in a radiological attack (Ferguson, 2003). The majority of these sources are included in the pre-programmed gamma spectrometry library for the detection system. The only source not in the library is $^{241}$Am, which was counted using a user-defined energy window. Some of the source characteristics and detection system properties used in the Monte Carlo modeling are presented in Table 3.1. Many of these sources have numerous photon

emissions in their decay schemes, but only the principal $\gamma$-rays and their corresponding region of interest (ROI) have been included. For the analysis of the $^{192}$Ir source, it should be noted that the gamma energy range and intensity represent six photons.

Table 3.1: Source Characteristics and Detection Properties

| Radionuclides | | Co-60 | I-131 | Cs-137 | Ir-192 | Am-241 |
|---|---|---|---|---|---|---|
| $\gamma$-ray | Energy (keV) | 1173 1333 | 364.5 637 | 661.7 | 296 – 612 | 59.5 |
| | Intensity | 1 1 | 0.81 0.073 | 0.851 | 2.1 | 0.359 |
| ROI (keV) | | 997-1533 | 309-420 | 561-761 | 250-703 | 40-73 |

In each of the models that follow, the response of the detection system will be calculated using the pulse-height tally available in MCNP. This tally summarizes the normalized number of photons interacting with the detector and is equivalent to the experimentally determined absolute efficiency of the thyroid probe, with units of counts-per-second per photon-per-second (Kramer et al., 2000).

### 3.2 Code and Model Validation

To ensure that the modeled detector and the MCNP code could effectively simulate the actual performance of the Atomlab system, a variety of simulations were performed for comparison with the measured data of SC&A. These measured data sets included point sources of radiation in air and in various depths in an acrylic slab phantom. An additional set of measurements were available for a distributed source in a water-filled phantom.

### 3.2.1 Point Sources in Air

The first measurements involved discrete, encapsulated sources of $^{60}Co$, $^{137}Cs$, $^{192}Ir$ and $^{241}Am$. These sources were individually placed at various distances from the NaI crystal, ranging from the face of the collimator to a position 100 cm from the end of the collimator. This setup was utilized to determine the response of the detection system to gamma-emitting sources that have not been greatly attenuated in a transport medium. The MCNP simulation of this design was modeled as exactly as possible, representing the small encapsulated sources as point sources.

### 3.2.2 Acrylic Slab Phantom

Further studies were performed using an acrylic slab phantom to simulate the transport of photons through a material with characteristics similar to that of human tissue. The slabs were composed of plastic, polymethyl-methacrylate (PMMA), with a typical density of 1.19 g/cm$^3$ and chemical formula $(C_5O_2H_8)_n$ (Anigstein et al., 2005). A total of ten slabs, each approximately 29.9 cm x 29.9 cm square with a thickness of 2.4 cm, were utilized in the original measurement program to simulate the effect of varying tissue thickness on the Atomlab's detection efficiency.

The same sources used in the air model were also used in this study. Each of the sealed sources was individually placed in an eleventh slab that had an air gap in the middle to hold the source. Anigstein et al. first performed measurements with the collimator flush against the source slab, then additional slabs were progressively added between the detector and source until all of the slabs had been analyzed (Figure 3.2).

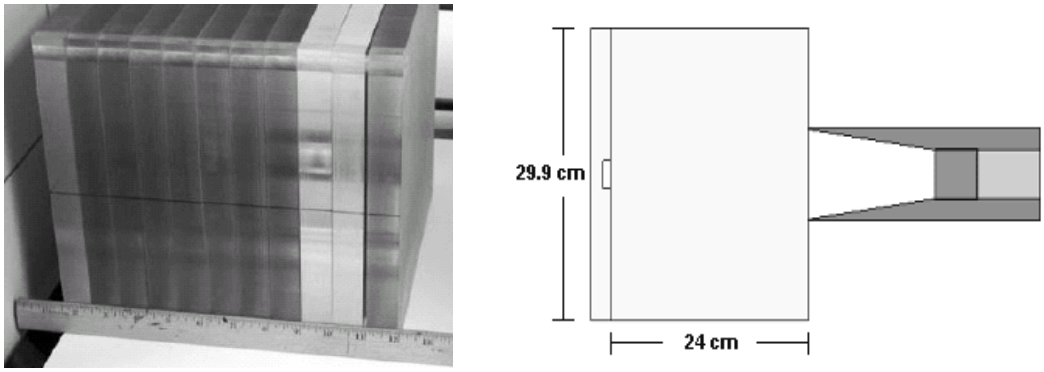


Figure 3.2: Full Acrylic Slab Phantom (Anigstein et al., 2005) and MCNP Visualization

When this model was created in MCNP5, it was to mimic the measurement program as closely as possible. The discrete sources, however, were again modeled as isotropic point sources, but an additional adjustment can be seen in Figure 3.2. Unlike the setup used by SC&A, all of the slabs other than the source-holder have been modeled as one continuous block. The slight separation or air gap that could exist between the slabs has been disregarded and is expected to have little, if any effect on simulated detection efficiency.

### 3.2.3 Water-Filled Phantom

The final setup analyzed with MCNP from the SC&A measurement program was the distributed source in a water-filled phantom. This design is supposed to mimic the expected source distribution for an inhalation model and will test the detector's response as a function of distance from the center of the source phantom. Two different orientations were used in this study with measurements made from both the broad and narrow sides of the phantom. Measurements were made with the phantom placed a number of distances from the detector, extending from the collimator face to 100 cm from the collimator.

The phantom used in the measurement program was a plastic jug with an aqueous solution of $^{131}I$ distributed in the water volume. The dimensions of the container were approximately 28 cm x 16 cm with a height of 38 cm, with the water in the system reaching a level of 28 cm (Erdman, 2005). The actual setup and MCNP representations are illustrated below in Figures 3.3 and 3.4 respectively, with the distributed source visible in the simulated model.

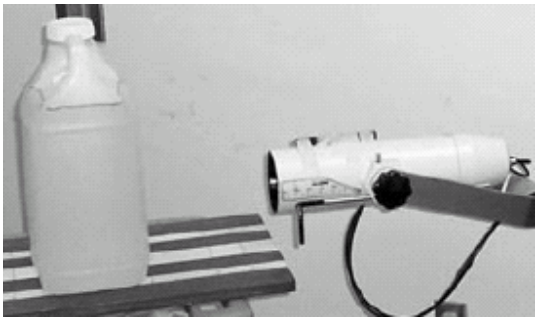

Figure 3.3: Water-Filled Phantom Setup (Anigstein et al., 2005)

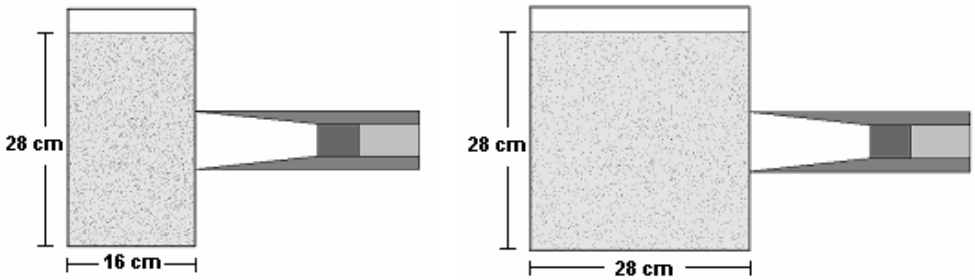


Figure 3.4: MCNP Visualization of Broad and Narrow Views of Water-Filled Phantom

### 3.3 Human Phantom Models

In an effort to extend the findings of the measurement study to include designs more realistic of the human body, anthropomorphic phantoms of several ages and body

sizes were created using the software package, BodyBuilder (White Rock Science, 2004). The human models developed in this program are based on the Medical Internal Radiation Dose (MIRD) reports and are generated into a MCNP geometry format (Van Riper, 2004). For the purpose of this study, phantoms representing a man, woman, adipose man, adipose woman and an androgynous 10-year-old child were created. Each of these models has varying lung sizes and chest thicknesses and better represent the human body as well as some variations in the general population, than would point sources and acrylic slabs. Dimensions of the phantoms are shown in Table 3.2.

Table 3.2: Human Phantom Statistics

| Phantom | Height (cm) | Weight (kg) | Lung Volume ($cm^3$) | Lung Height (cm) | Chest to Lung Position (cm) | | |
|---|---|---|---|---|---|---|---|
| | | | | | Front Edge | Center Lung | Back Edge |
| Man | 179 | 73.1 | 3380 | 24.0 | 2.8 | 9.3 | 15.8 |
| Woman | 168 | 56.5 | 2200 | 20.6 | 3.0 | 9.1 | 15.2 |
| Adipose Man | 179 | 113 | 3380 | 24.0 | 7.8 | 14.3 | 20.8 |
| Adipose Woman | 168 | 89.5 | 2200 | 20.6 | 8.1 | 14.2 | 20.3 |
| Androgynous Child | 140 | 32.7 | 1530 | 17.4 | 2.3 | 7.7 | 13.2 |

In these phantoms, both distributed and point sources of radiation have been modeled. The sources that were analyzed were the same used in the validation models, which included $^{60}Co$, $^{131}I$, $^{137}Cs$, $^{192}Ir$ and $^{241}Am$. In the phantom simulations, the isotropic point sources were individually placed in the center of each lung and were each assigned the same intensity. For the distributed source models, the starting location and direction of the photons are established in the lung volumes at random by the Monte Carlo code. This is accomplished by enclosing the source organ in the smallest box that

will completely contain it and choosing points at random within the box that also lie within the lungs. If the point does not lie in either of the lungs, it is rejected and another emission point is chosen (Stansbury, 1994). This process is repeated until a predetermined number of particle histories have been simulated. Several illustrations of the phantom models, source distributions, and detector placement are shown in Figure 3.5.

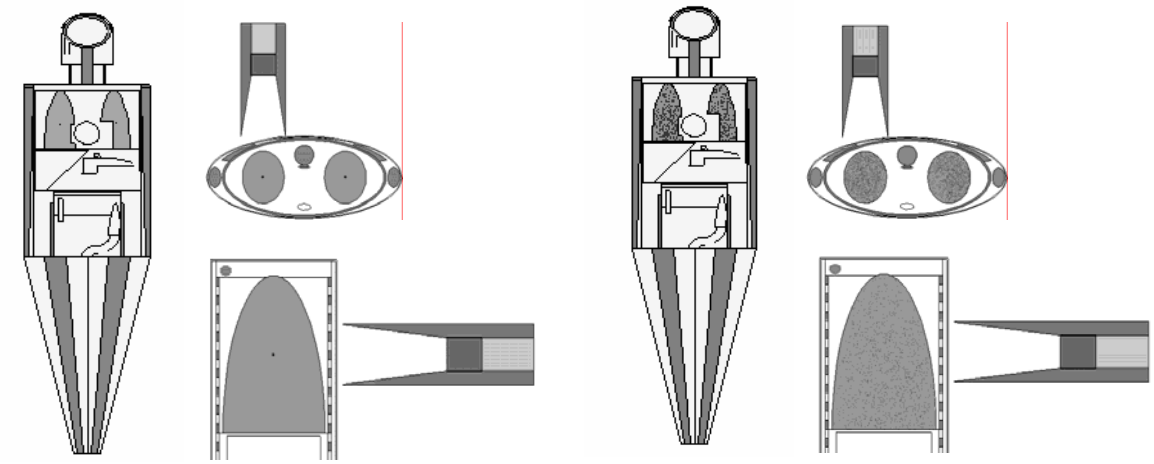

Figure 3.5: Human Phantom and Detector Models for Point and Distributed Sources

The physical placement of the thyroid probe can greatly influence the detection efficiency. In regard to Figure 3.5, it can be seen that the collimated detection system is not large enough to monitor both lungs at the same time, a problem not usually encountered in a dedicated WBC system. To address this issue, several preliminary MCNP simulations were made to determine the optimal positioning for the detector before fully analyzing each phantom and source distribution.

In these scoping calculations, the detector was modeled at center-lung height and at positions on both the front and the back of the phantom. A total of five locations were analyzed with the detector centered on each lung from the front, each lung from the back, and a fifth position on the chest, in between the two lungs. A distributed source was used in each case and both collimated and uncollimated systems were simulated to examine the effects related to detector geometry, even though the Atomlab 950 is only operated as a collimated system. The results are presented in Figure 3.6 where the relative detection efficiency was calculated by dividing the results for each detection position by the highest efficiency for the collimated and uncollimated detector geometry.

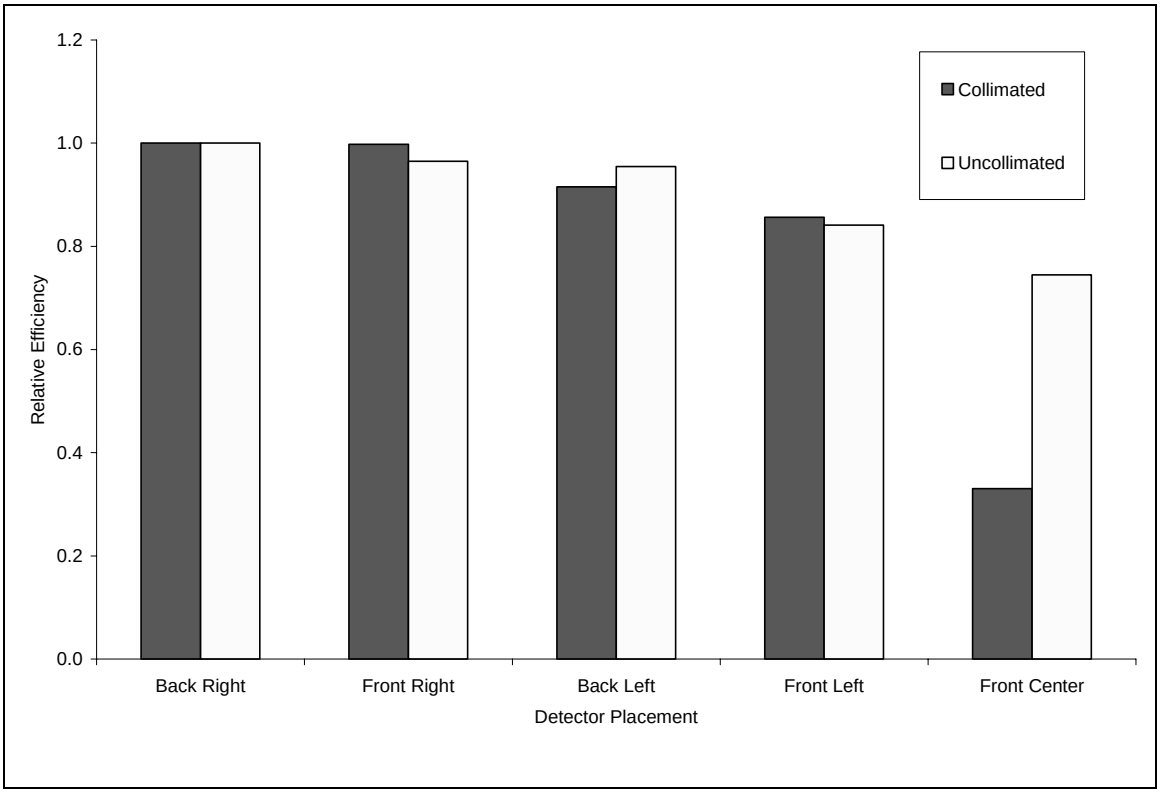


Figure 3.6: Relative Efficiency vs. Detector Placement for a Distributed Source in a Male Phantom

From these data, it is evident that positioning the detector over the phantom's right lung from either the front or the back would provide the highest count rate. However, due to anatomical differences that exist between some of the phantoms and the desire to develop standardized models that can be applied to a variety of setups, all the simulations were performed with the thyroid probe from the back, right lung position.

An additional conclusion can be drawn from the results in Figure 3.6 in regard to the collimation of the system. Since the data are normalized to the highest efficiency, it is hard to distinguish the gain in efficiency when the system is placed over the lungs. However, the results for the center chest position indicate that a rather substantial increase will be obtained by utilizing an uncollimated system, an example of which is presented in Figure 3.7.

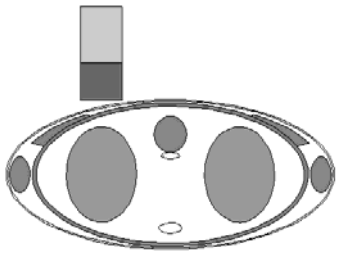

Figure 3.7: Position of an Uncollimated Detector on a Male Phantom

Previously, the collimator shielded the detector from most of the lungs as well as increased the distance to the source by an additional 15 cm. Without the collimator present, however, there will be an increase in background counts that could adversely affect the MDA of the thyroid probe.

### 3.4 Minimum Detectable Activity and Dose Correlations

Factors such as the background count rate and the detector count time can greatly influence the performance of any *in vivo* monitoring system. Therefore, it is necessary to establish a detection limit based on the characteristics of the system in question to effectively assay radioactivity. For this work, a number of source distributions and detector geometries have been analyzed. The ability to identify low levels of activity for each of these setups will be valuable in assessing the capability of the thyroid probe to function as a lung monitor.

Although many definitions have existed for this limit, the minimum detectable activity (MDA) can be best described as the smallest amount of activity that can be distinguished from background, given a certain confidence level (Steinmeyer, 1998). The concepts behind this definition are primarily based on the work of Currie, who established theoretical levels for detection using Poisson statistics to approximate the counting of radioactive samples (Currie, 1968). A basic equation for determining the MDA of a detector is:

$$\mathrm{MDA} = \frac{3 + 4.65\sqrt{B \cdot t_b}}{t_c \cdot \varepsilon} \qquad [3.1]$$

where:

B = background counting rate in the ROI (cpm)

$\varepsilon$ = detection efficiency for a specific nuclide ($cpm \cdot nCi^{-1}$)

$t_b$ = counting time for background (min)

$t_c$ = counting time for measurement (min)

The MDA described by this equation refers to the minimal activity that will be detected 95% of the time. For values below this limit the presence of activity can not be accurately measured, but activity above background levels may still exist. In this study, the efficiency will be determined directly from the MCNP output for each of the phantom setups and the counting times for the background and measurement are assumed to be the same.

For the collimated detector models, the background count rates used in the MDA calculations were obtained from SC&A's results. Since the collimator could not be removed in their study (Erdman, 2005), another method was used to obtain an uncollimated background. The Veterans Affairs Medical Clinic in Atlanta uses a similar thyroid uptake system with the same NaI crystal size which could be removed from the lead collimator housing. The background count rate obtained from this detector has been used in the analysis of the MDA for the uncollimated system.

In applying these results to an inhalation model, the retention of the radioactive material in the lungs over time must be considered. After just several hours from intake, only a fraction of the inhaled material will still remain in the lungs and will further influence the detection ability as time progresses. It is therefore important to monitor internally contaminated victims as quickly as possible following an RDD event.

An estimate of the committed dose that would be obtained as a result of insufficient detection capabilities can be determined by applying dose conversion coefficients (DCCs) to the MDA values. These dose coefficients utilize radioactive decay properties, biokinetic models, as well as inhaled particle size to determine the dose over a 50-year period following intake. To account for the migration of contaminants

from the lungs prior to assay, intake retention fractions (IRFs) from NUREG/CR-4884 have been utilized (Lessard et. al., 1987) and are listed in Tables 4.4 through 4.9. The DCCs presented in Table 3.3 were obtained from Federal Guidance Report No.11 and yield the highest committed effective dose for the particle classes listed. These classifications describe the lung clearance times which may be on the order of days (D), weeks (W), or years (Y), depending on the radionuclide in question. For this analysis, the inhaled particle sizes are 1-μm activity median aerodynamic diameter (AMAD).

Table 3.3: Effective Dose Conversion Coefficients for Several Radionuclides of Interest

| Radionuclide | Co-60 | I-131 | Cs-137 | Ir-192 | Am-241 |
|---|---|---|---|---|---|
| Particle Class | Y | D | D | Y | W |
| DCC [$h_{e(50)}$] (mrem/nCi) | 0.219 | .0329 | .0319 | 0.0282 | 444.0 |

It should be noted for $^{241}$Am that the DCC is at least three orders of magnitude larger than the other isotopes being considered. This value, however, is not the controlling dose for the annual limit of intake (ALI) for $^{241}$Am. For this isotope, the ALI is based on a 50 rem committed dose equivalent (CDE) to the bone surface (PNNL, 2003). In place of the dose coefficient listed in Table 3.3, the CDE of 8.03 rem/nCi has been implemented to account for the bone surface limitation (EPA, 1988).

# CHAPTER 4

# RESULTS

## 4.1 Validation Models

The goal of the validation models was to ensure that MCNP could accurately reproduce results that were experimentally measured. For the point source measurements in air, 10 million particle histories were tracked and results were obtained with average statistical uncertainty of less than 2%. A comparison of these models is presented in Figure 4.1, where the ratio of the measured data to the MCNP results is plotted against the source-detector distance.

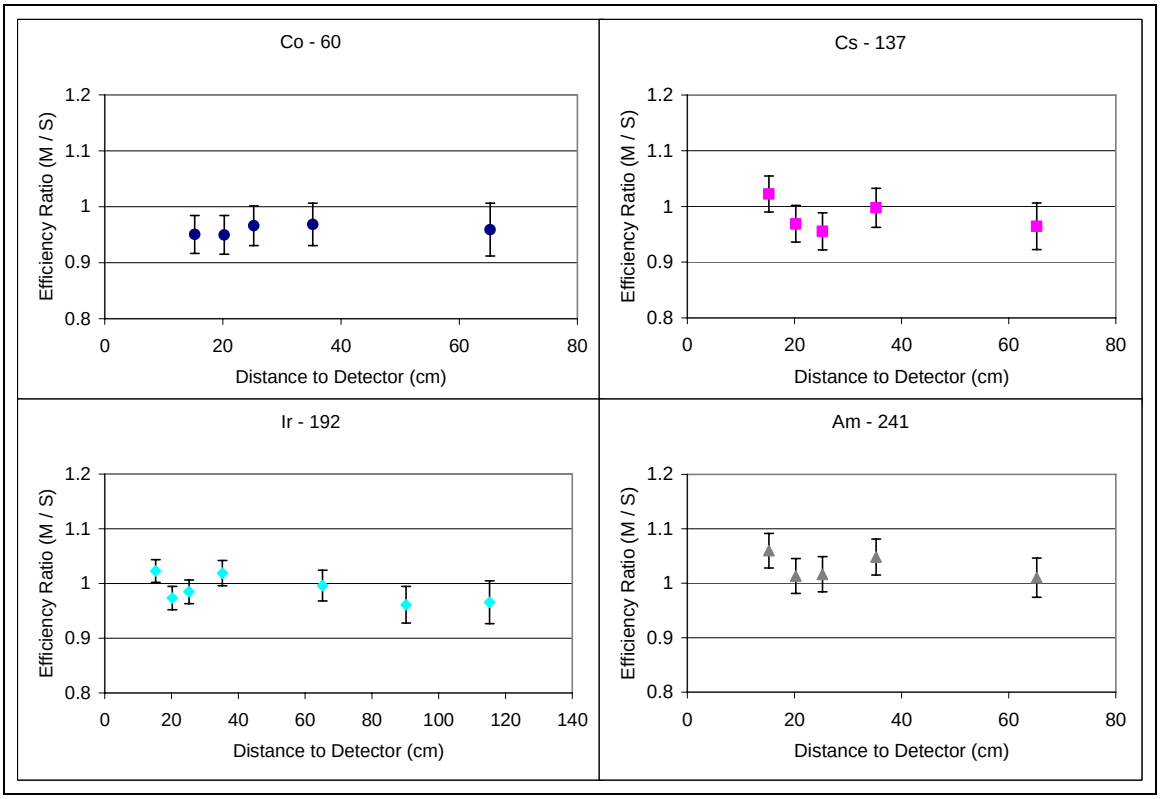


Figure 4.1: Ratio of Measured Values (M) to MCNP Simulations (S) for Point Sources in Air at Various Distances from the Detector

As can be seen in Figure 4.1, the MCNP results compare well with the measured values where the uncertainties in the models have been propagated using standard error analysis. It should be noted that point source measurements for $^{131}I$ were not made in the measurement program and were therefore unavailable for comparison in the air and slab models.

In the acrylic slab phantom measurements, the number of particle histories was increased to 50 million to ensure the photon transport through the absorbing medium would not result in an increased error value. The comparison between the MCNP and measured results are presented in Figure 4.2 and the statistical uncertainty for these simulations was under 1% for all of the sources and slab geometries.

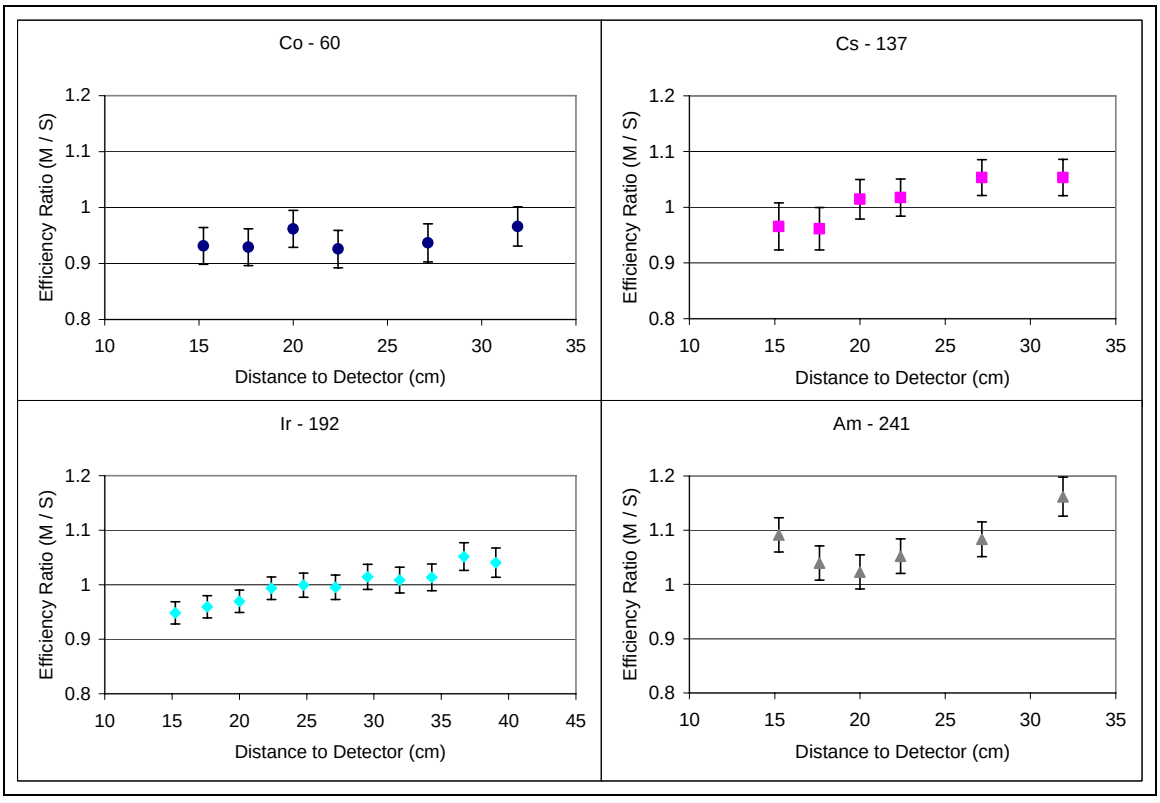


Figure 4.2: Ratio of Measured Values (M) to MCNP Simulations (S) for Point Sources at Various Depths in a Slab Phantom

As indicated in Figure 4.2, the MCNP results were again comparable to the measured values. It should be noted for both the point and acrylic slab models that more data points were available for $^{192}$Ir than for the other sources. This is due to the high activity of the iridium sample used in SC&A's measurement program; measurements could be made in thicker slab geometries and at distances further from the detector.

The final validation model tested the response of the detector to a diffuse source of radioactivity, corresponding to the measurements of $^{131}$I in Chapter 3. In this water-phantom model, 50 million particle histories were tracked, with an average statistical uncertainty of approximately 1.5%.

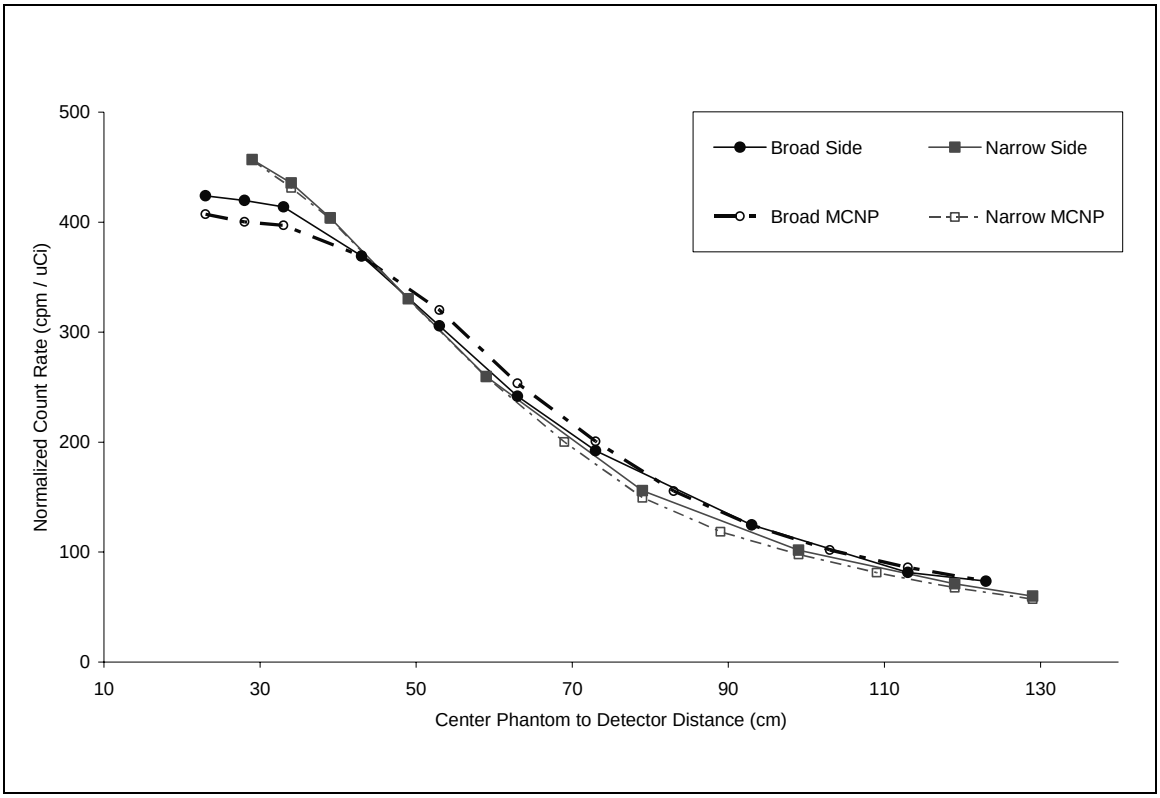


Figure 4.3: Distributed $^{131}$I Source in Water-Filled Phantom, Measurements vs. MCNP

It can be seen in Figure 4.3 that the narrow-sided measurement initially produces a higher count rate because more of the source is viewed by the detector. However, at about 45 cm the impact of the collimator is no longer seen as both narrow and broad views produce similar results.

### 4.2 Detection Efficiency for Human Phantoms

In the human phantom models, several different factors have been analyzed along with their influence on the thyroid probe's detection efficiency. These included different source distributions, detector geometries, and tissue thicknesses that would be encountered in an RDD event. In each of the simulations, 100 million particle histories were tracked, and the statistical uncertainty ranged from a few tenths to 1%.

The data presented in Figures 4.4 through 4.13 are listed according to radionuclide and have been grouped based on the collimation and source distribution of the model. For the collimated detectors, the point source in the lung resulted in higher efficiencies than did the distributed source for the same total activity. This can be attributed to the collimator limiting the view of the detector. Not all of the source material in the lungs of the phantoms was visible to the NaI crystal in the distributed source case, whereas for the point source, the detector was directly in line with the source. However, for larger phantoms, the efficiencies for the point source and distributed source approach one another. It should also be noted that the efficiencies in every case decrease from the highest value, obtained in the child, down to the adipose man. The differences among these phantoms are presented in Table 3.2.

In the following set of results, a second figure for each radionuclide compares the detection efficiencies between a collimated and uncollimated detector. Depending on the

source and the phantom of interest, the efficiency gained in using an uncollimated system can range from a factor of 5 for $^{60}$Co uniformly distributed in an adipose woman to a factor of 12 for $^{241}$Am distributed in a child's lungs. As mentioned previously, this setup will have a larger background count rate, the effect of which will be analyzed in Section 4.3.

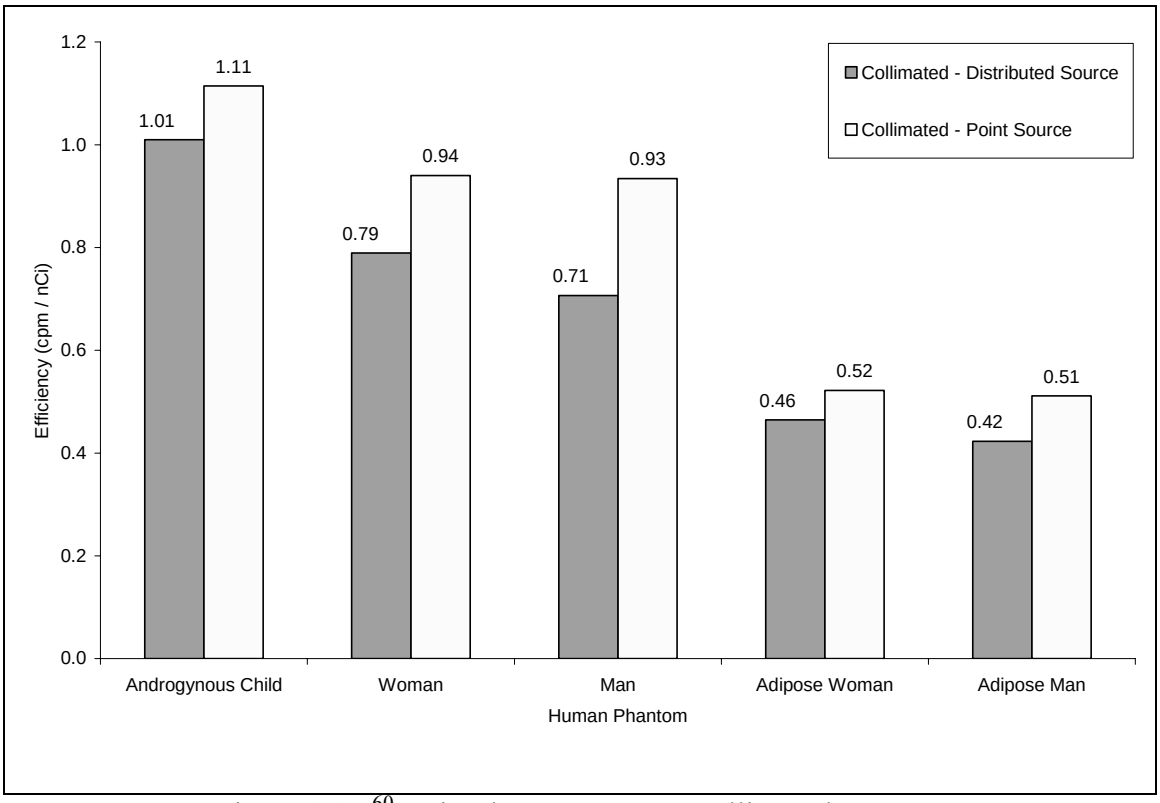


Figure 4.4: $^{60}$Co in Phantom Lungs, Collimated Detector

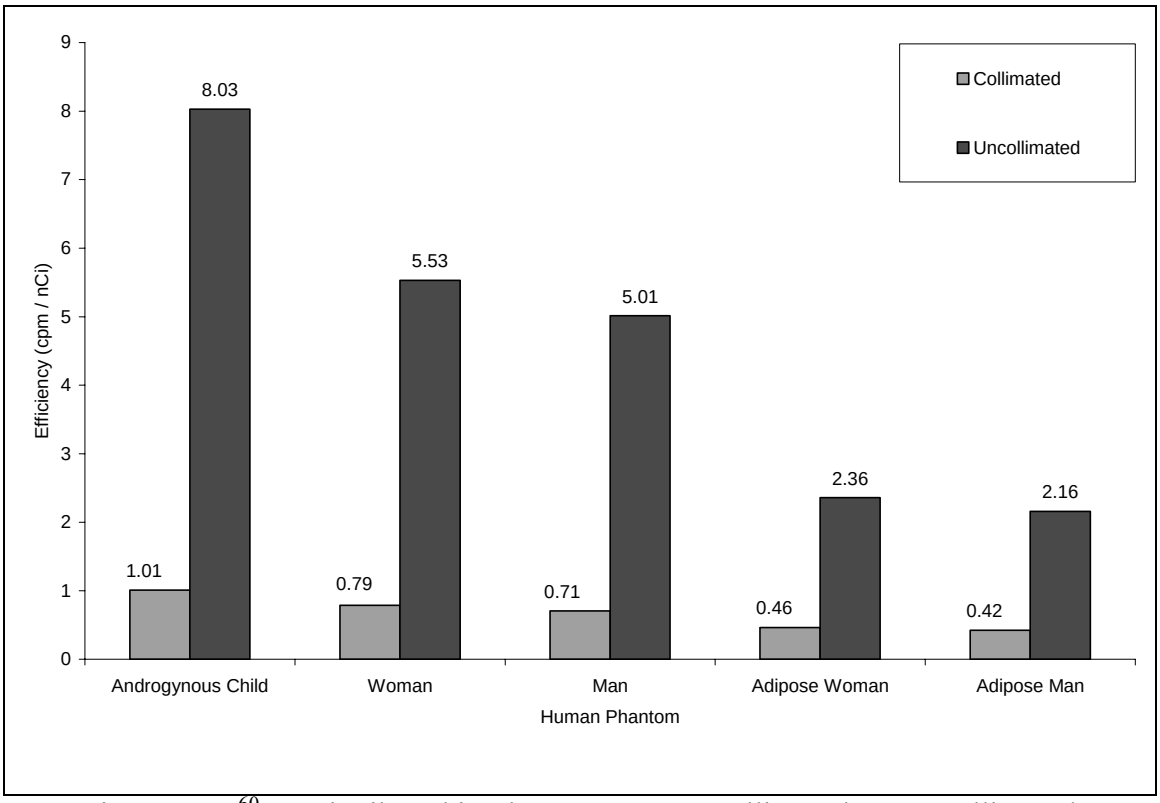


Figure 4.5: $^{60}$Co Distributed in Phantom Lungs, Collimated vs. Uncollimated

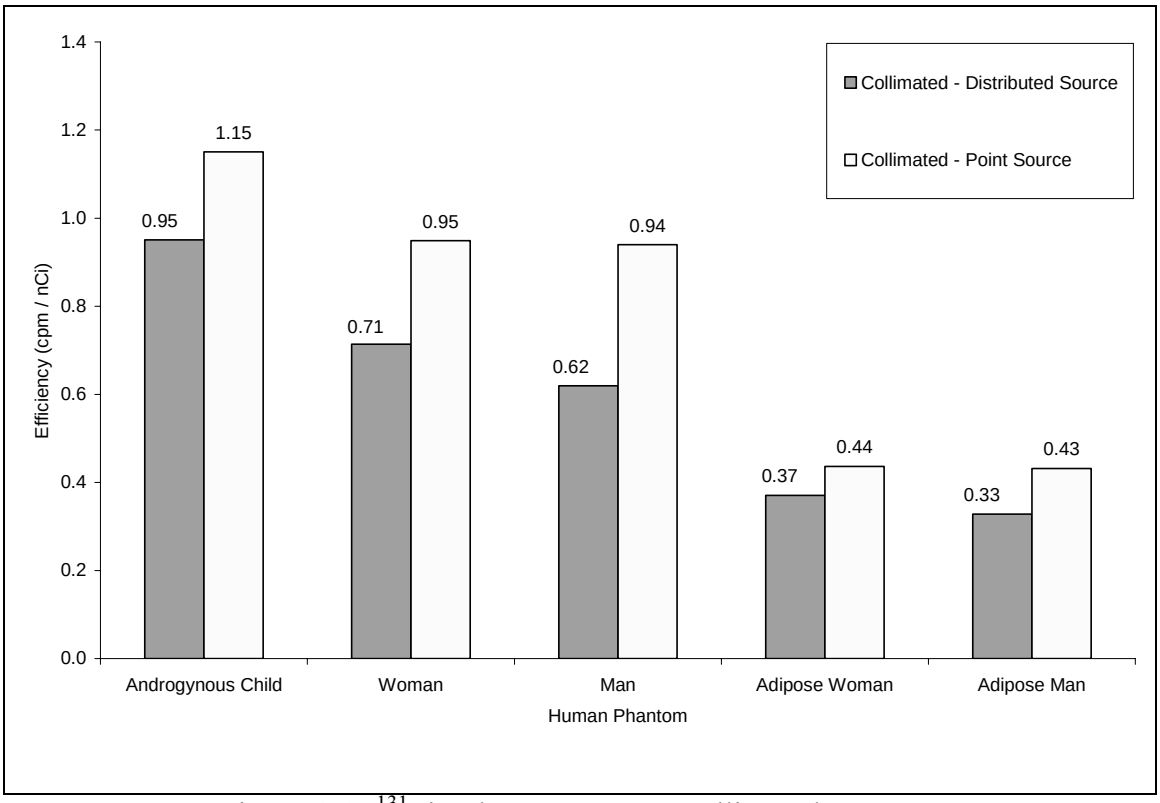


Figure 4.6: $^{131}$I in Phantom Lungs, Collimated Detector

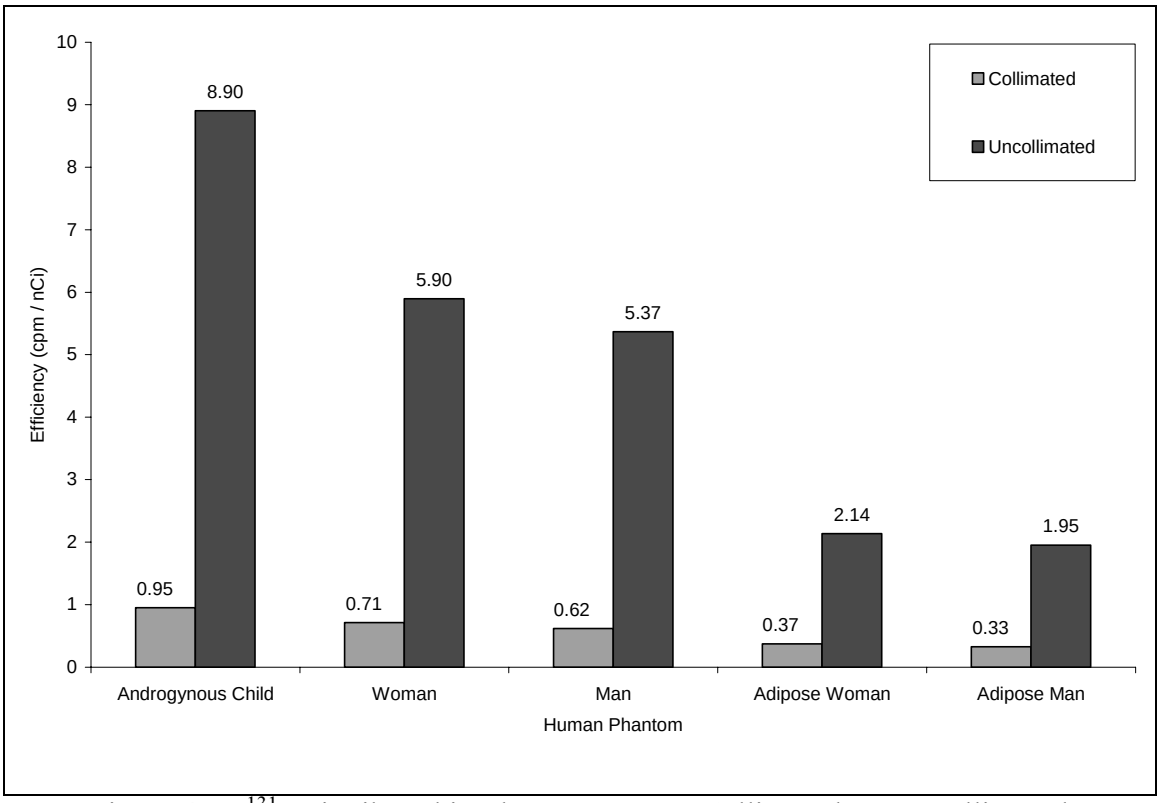


Figure 4.7: $^{131}$I Distributed in Phantom Lungs, Collimated vs. Uncollimated

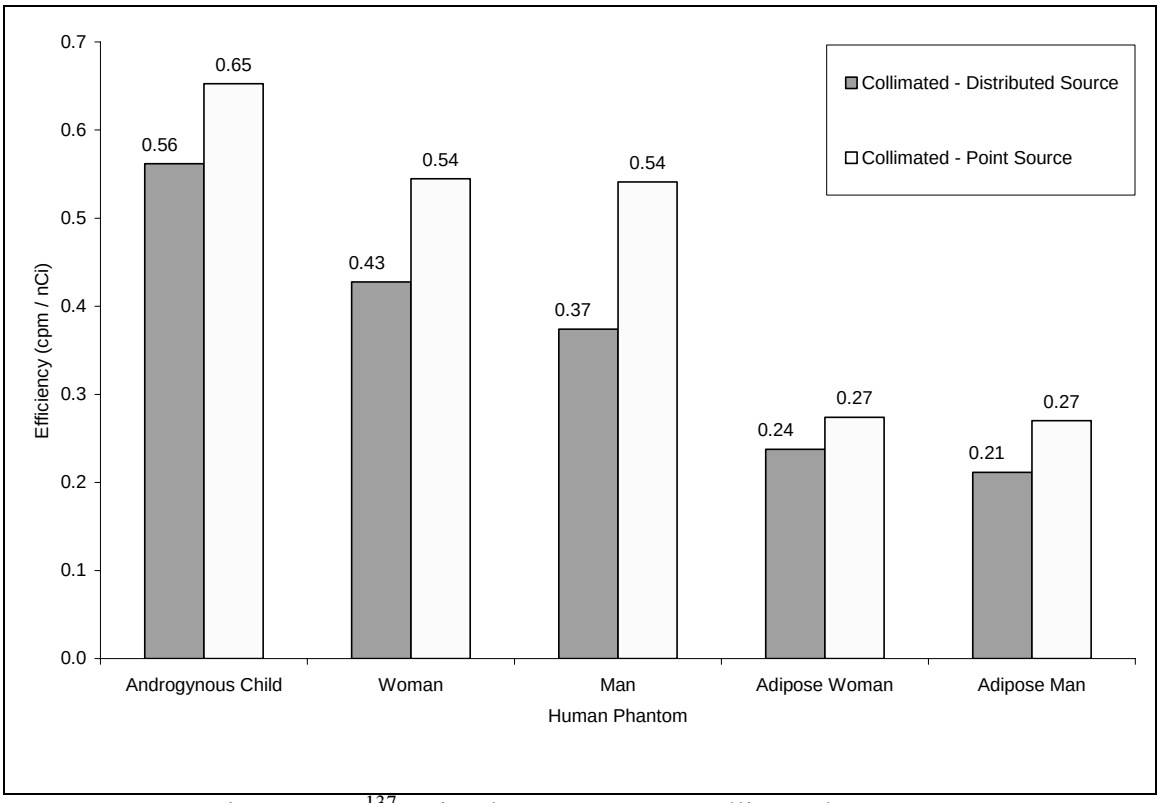


Figure 4.8: $^{137}$Cs in Phantom Lungs, Collimated Detector

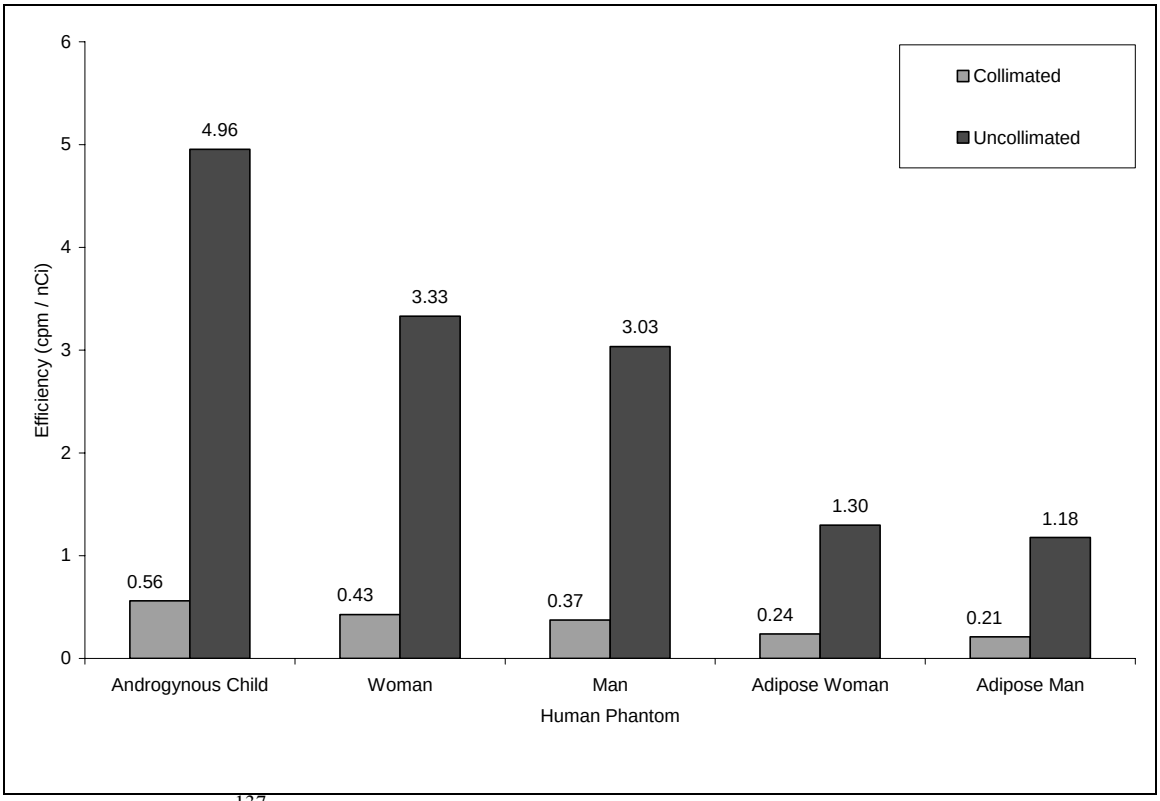


Figure 4.9: $^{137}$Cs Distributed in Phantom Lungs, Collimated vs. Uncollimated

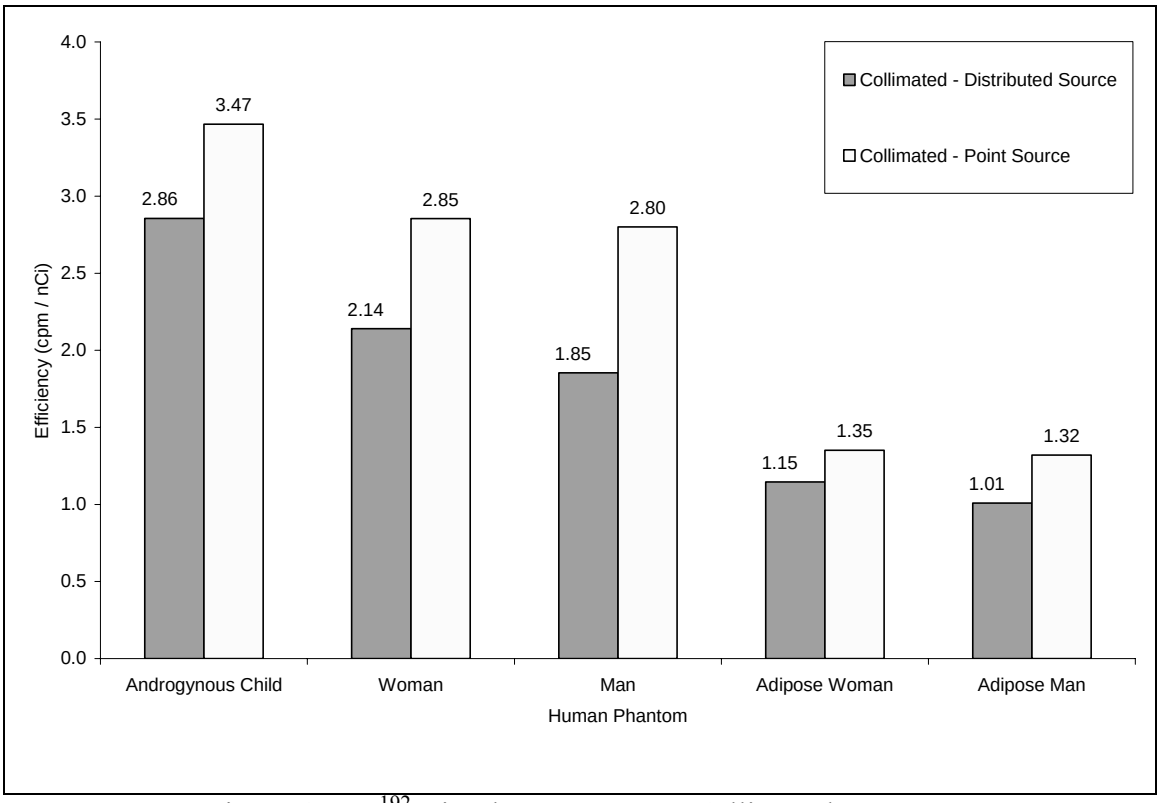


Figure 4.10: $^{192}$Ir in Phantom Lungs, Collimated Detector

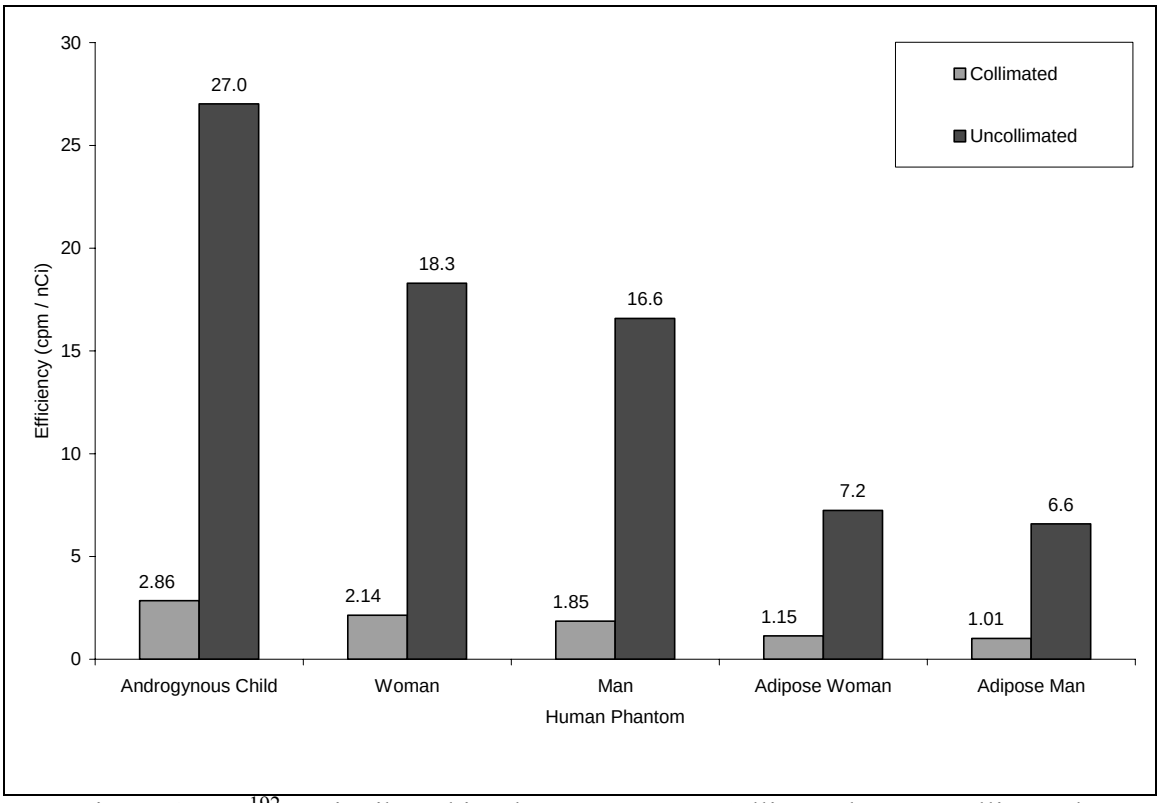


Figure 4.11: $^{192}$Ir Distributed in Phantom Lungs, Collimated vs. Uncollimated

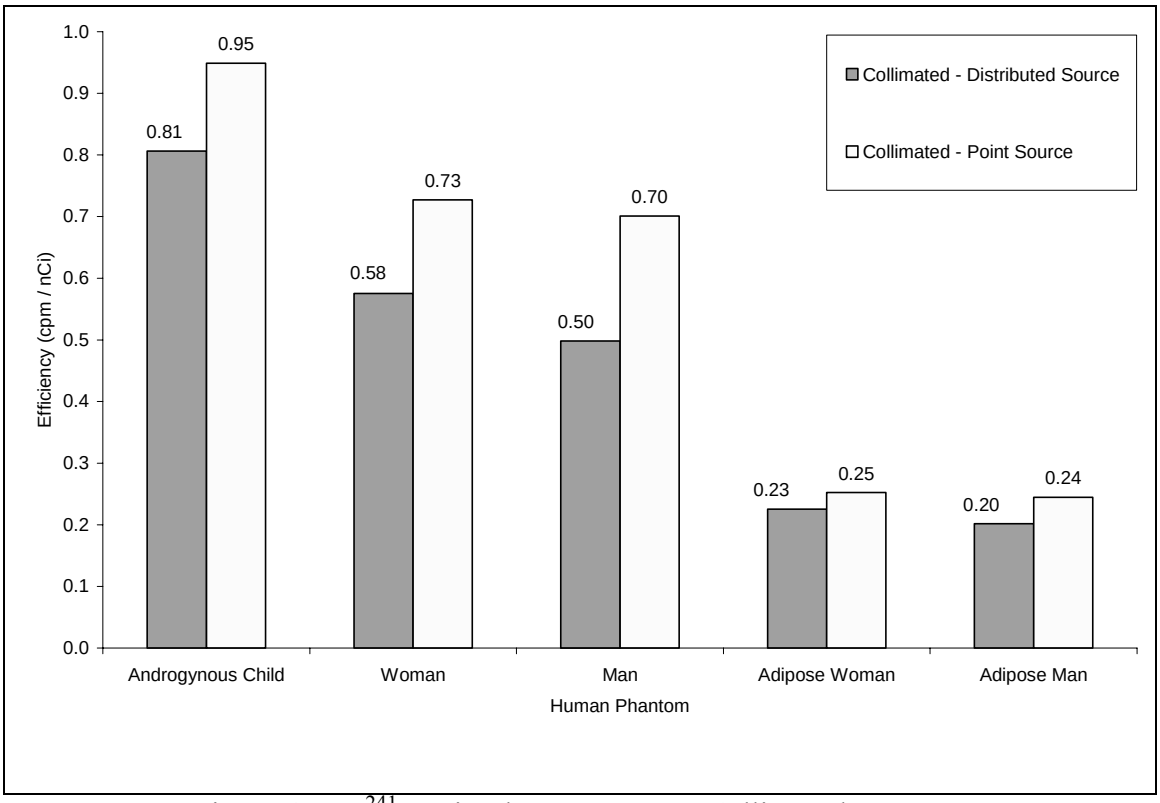


Figure 4.12: $^{241}$Am in Phantom Lungs, Collimated Detector

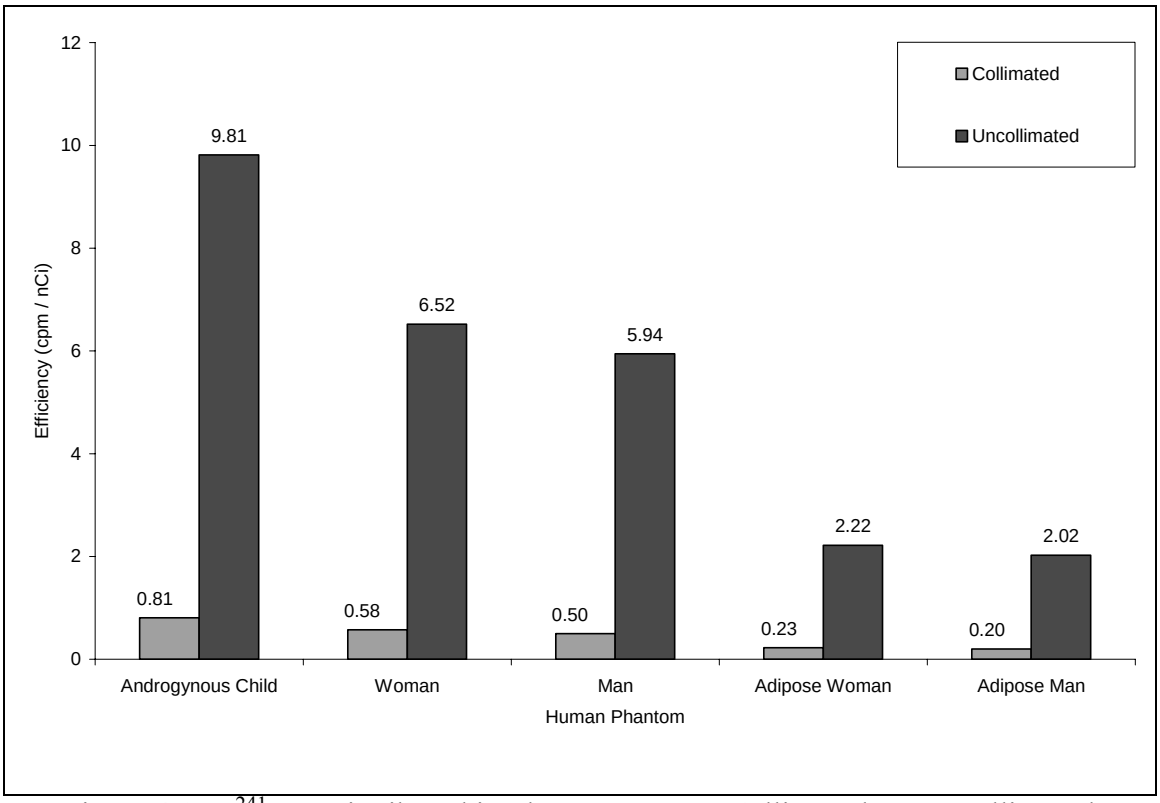


Figure 4.13: $^{241}$Am Distributed in Phantom Lungs, Collimated vs. Uncollimated

### 4.3 Minimum Detectable Activity

The MDA of the thyroid probe has been calculated for numerous scenarios using Equation 3.1. Tables 4.1 through 4.3 present the results for each of the radionuclides examined and illustrate the effects that counting time, source distribution, and detector geometry can have on the detectable activity. The MDA developed by SC&A is also analyzed with results presented in Figure 4.14.

Table 4.1: MDA vs. Counting Time for Distributed Sources in the Lungs of Anthropomorphic Phantoms, Using a Collimated Detector

| Nuclide | Background (cpm) | Phantom | Detector Efficiency (cpm/nCi) | Counting Time (min) & MDA (nCi) | | | |
|---|---|---|---|---|---|---|---|
| | | | | 1 | 3 | 5 | 10 |
| Co-60 | 56 | AC | 1.01 | 37.4 | 20.9 | 16.0 | 11.2 |
| | | W | 0.79 | 47.9 | 26.7 | 20.5 | 14.3 |
| | | M | 0.71 | 53.5 | 29.8 | 22.9 | 16.0 |
| | | AW | 0.46 | 81.4 | 45.4 | 34.8 | 24.3 |
| | | AM | 0.42 | 89.4 | 49.9 | 38.2 | 26.7 |
| I-131 | 52 | AC | 0.95 | 38.4 | 21.4 | 16.4 | 11.5 |
| | | W | 0.71 | 51.2 | 28.5 | 21.9 | 15.3 |
| | | M | 0.62 | 58.9 | 32.9 | 25.2 | 17.6 |
| | | AW | 0.37 | 98.5 | 54.9 | 42.1 | 29.4 |
| | | AM | 0.33 | 111 | 62.1 | 47.5 | 33.2 |
| Cs-137 | 62 | AC | 0.56 | 70.5 | 39.4 | 30.2 | 21.1 |
| | | W | 0.43 | 92.6 | 51.8 | 39.7 | 27.8 |
| | | M | 0.37 | 106 | 59.2 | 45.4 | 31.8 |
| | | AW | 0.24 | 167 | 93.2 | 71.4 | 50.0 |
| | | AM | 0.21 | 187 | 104.7 | 80.3 | 56.2 |
| Ir-192 | 186 | AC | 2.86 | 23.3 | 13.2 | 10.1 | 7.1 |
| | | W | 2.14 | 31.0 | 17.6 | 13.5 | 9.5 |
| | | M | 1.85 | 35.8 | 20.3 | 15.6 | 11.0 |
| | | AW | 1.15 | 58.0 | 32.8 | 25.3 | 17.8 |
| | | AM | 1.01 | 65.8 | 37.3 | 28.7 | 20.2 |
| Am-241 | 34 | AC | 0.81 | 37.3 | 20.7 | 15.8 | 11.0 |
| | | W | 0.58 | 52.3 | 29.0 | 22.1 | 15.4 |
| | | M | 0.50 | 60.4 | 33.4 | 25.5 | 17.8 |
| | | AW | 0.23 | 134 | 73.8 | 56.4 | 39.3 |
| | | AM | 0.20 | 149 | 82.6 | 63.1 | 44.0 |

Where:
M – Man W – Woman AC – Androgynous Child
AM – Adipose Man AW – Adipose Woman

Table 4.2: MDA vs. Counting Time for Point Sources in the Lungs of Anthropomorphic Phantoms, Using a Collimated Detector

| Nuclide | Background (cpm) | Phantom | Detector Efficiency (cpm/nCi) | Counting Time (min) & MDA (nCi) | | | |
|---|---|---|---|---|---|---|---|
| | | | | 1 | 3 | 5 | 10 |
| Co-60 | 56 | AC | 1.11 | 33.9 | 18.9 | 14.5 | 10.1 |
| | | W | 0.94 | 40.2 | 22.4 | 17.2 | 12.0 |
| | | M | 0.93 | 40.5 | 22.6 | 17.3 | 12.1 |
| | | AW | 0.52 | 72.4 | 40.4 | 31.0 | 21.7 |
| | | AM | 0.51 | 73.9 | 41.2 | 31.6 | 22.1 |
| I-131 | 52 | AC | 1.15 | 31.8 | 17.7 | 13.6 | 9.5 |
| | | W | 0.95 | 38.5 | 21.5 | 16.4 | 11.5 |
| | | M | 0.94 | 38.9 | 21.7 | 16.6 | 11.6 |
| | | AW | 0.44 | 83.7 | 46.7 | 35.7 | 25.0 |
| | | AM | 0.43 | 84.7 | 47.2 | 36.1 | 25.3 |
| Cs-137 | 62 | AC | 0.65 | 60.7 | 33.9 | 26.0 | 18.2 |
| | | W | 0.54 | 72.7 | 40.6 | 31.2 | 21.8 |
| | | M | 0.54 | 73.2 | 40.9 | 31.4 | 22.0 |
| | | AW | 0.27 | 145 | 80.8 | 61.9 | 43.3 |
| | | AM | 0.27 | 147 | 82.0 | 62.9 | 44.0 |
| Ir-192 | 186 | AC | 3.47 | 19.2 | 10.8 | 8.4 | 5.9 |
| | | W | 2.85 | 23.3 | 13.2 | 10.1 | 7.1 |
| | | M | 2.80 | 23.7 | 13.4 | 10.3 | 7.3 |
| | | AW | 1.35 | 49.1 | 27.8 | 21.4 | 15.1 |
| | | AM | 1.32 | 50.3 | 28.5 | 21.9 | 15.4 |
| Am-241 | 34 | AC | 0.95 | 31.7 | 17.6 | 13.4 | 9.4 |
| | | W | 0.73 | 41.4 | 22.9 | 17.5 | 12.2 |
| | | M | 0.70 | 43.0 | 23.8 | 18.2 | 12.7 |
| | | AW | 0.25 | 119 | 66.0 | 50.4 | 35.2 |
| | | AM | 0.24 | 123 | 68.2 | 52.1 | 36.3 |

Where:
M – Man W – Woman AC – Androgynous Child
AM – Adipose Man AW – Adipose Woman

Table 4.3: MDA vs. Counting Time for Distributed Sources in the Lungs of Anthropomorphic Phantoms, Using an Uncollimated Detector

| Nuclide | Background (cpm) | Phantom | Detector Efficiency (cpm/nCi) | Counting Time (min) & MDA (nCi) | | | |
|---|---|---|---|---|---|---|---|
| | | | | 1 | 3 | 5 | 10 |
| Co-60 | 395 | AC | 8.03 | 11.9 | 6.8 | 5.2 | 3.7 |
| | | W | 5.53 | 17.3 | 9.8 | 7.6 | 5.3 |
| | | M | 5.01 | 19.0 | 10.8 | 8.4 | 5.9 |
| | | AW | 2.36 | 40.4 | 23.0 | 17.8 | 12.5 |
| | | AM | 2.16 | 44.2 | 25.2 | 19.4 | 13.7 |
| I-131 | 923 | AC | 8.90 | 16.2 | 9.3 | 7.2 | 5.1 |
| | | W | 5.90 | 24.5 | 14.0 | 10.8 | 7.6 |
| | | M | 5.37 | 26.9 | 15.4 | 11.9 | 8.4 |
| | | AW | 2.14 | 67.6 | 38.7 | 29.9 | 21.1 |
| | | AM | 1.95 | 73.9 | 42.3 | 32.7 | 23.0 |
| Cs-137 | 449 | AC | 4.96 | 20.5 | 11.7 | 9.0 | 6.3 |
| | | W | 3.33 | 30.5 | 17.4 | 13.4 | 9.4 |
| | | M | 3.03 | 33.5 | 19.1 | 14.7 | 10.4 |
| | | AW | 1.30 | 78.2 | 44.6 | 34.4 | 24.2 |
| | | AM | 1.18 | 86.2 | 49.1 | 37.9 | 26.7 |
| Ir-192 | 2633 | AC | 27.02 | 8.9 | 5.1 | 4.0 | 2.8 |
| | | W | 18.30 | 13.2 | 7.6 | 5.9 | 4.1 |
| | | M | 16.58 | 14.6 | 8.4 | 6.5 | 4.6 |
| | | AW | 7.25 | 33.3 | 19.2 | 14.8 | 10.5 |
| | | AM | 6.59 | 36.7 | 21.1 | 16.3 | 11.5 |
| Am-241 | 1559 | AC | 9.81 | 19.0 | 10.9 | 8.4 | 5.9 |
| | | W | 6.52 | 28.6 | 16.4 | 12.7 | 9.0 |
| | | M | 5.94 | 31.4 | 18.0 | 13.9 | 9.8 |
| | | AW | 2.22 | 84.2 | 48.3 | 37.3 | 26.3 |
| | | AM | 2.02 | 92.2 | 52.8 | 40.8 | 28.8 |

Where:
M – Man W – Woman AC – Androgynous Child
AM – Adipose Man AW – Adipose Woman

Following from Equation 3.1, it is evident that an increase in the counting time will ultimately lower the MDA in every scenario. It can also be seen that the androgynous child phantom consistently yields the lowest MDA, as would be expected with the smaller chest thickness and distance to center lung. In Table 4.3 it has been shown that the effect of the increased background for the uncollimated detector was outweighed by the increased detection efficiency that came from the relocation of the NaI crystal closer to the phantom's back. The results for an uncollimated thyroid probe

indicate that it would provide the lowest MDA, but the influence of varying background count rates has not be analyzed.

### 4.3.1 Comparison to SC&A Model

In an effort to compare their results to an actual RDD scenario, SC&A correlated the measurements in their study to a distributed source in a lung (Anigstein et al., 2005). The MDA values obtained have been compared to the MCNP results for the collimated detector with distributed sources in the lungs of a male phantom. The results are presented in Figure 4.14, where the MDA ratio has been computed by dividing the SC&A measured values by those obtained with MCNP for the adult male phantom.

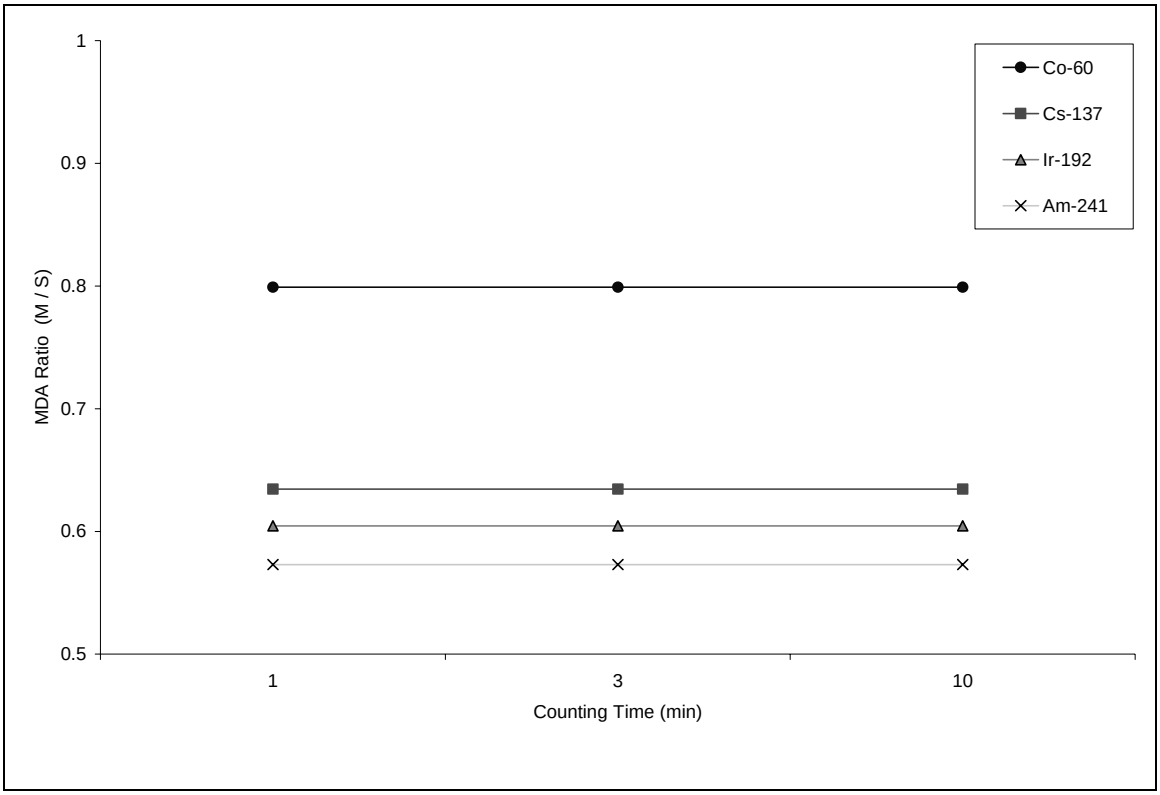


Figure 4.14: Ratio of Measured Values (M) to MCNP Simulations (S) for the MDA of Distributed Sources in the Lungs

From Figure 4.14, it can be seen that the method used in the measurement program overestimates the sensitivity of the detection system. In their analysis, SC&A evaluated the mass thickness of a theoretical phantom's chest wall and lung tissue to determine the number of acrylic slabs that would have a similar attenuation. To account for a distributed source in the phantom's lung, the results for $^{131}I$ in the water-filled jug were applied to the source-detector distance correlation. A correction factor was established from these data and was applied to the MDA values for the sources presented in Figure 4.14 to estimate the values for a distributed source (Anigstein et al., 2005).

The difference between SC&A's results and the MCNP values is particularly evident for the sources with lower energy photons, where a simple correlation will not effectively represent their transport through tissue. The only source for which values were somewhat similar for both MCNP and the measurement study was $^{60}Co$, whose high energy gammas will not be greatly attenuated in either model. $^{131}I$ was not available for comparison since SC&A did not have point source measurements for this radioisotope. It can be concluded that the MCNP simulations better represent source and phantom geometries that would be expected in an inhalation event and can therefore effectively predict the response of the thyroid counter to a variety of different scenarios.

## 4.4 Dose Calculations

The calculation of the committed dose has been performed for the radionuclides used in this work in regard to the male phantom. Since the amount of material in the lungs will decrease from the time of intake to the time of measurement, there is a possibility that only values below the MDA will be present when the person's lung is

assayed. Therefore, retention factors were used to determine activity on intake that must occur to obtain the MDAs at various times after the intake:

$$\mathrm{MDI} = \frac{\mathrm{MDA}}{\mathrm{IRF(t)}} \qquad [4.1]$$

where:

MDI = minimum detectable intake

MDA = minimum detectable activity (detection system)

IRF(t) = intake retention fraction (varies with time)

The dose coefficients from Table 3.3 were then applied to these intake values to determine the minimum detectable dose (MDD) that would be incurred from the initial inhaled activity:

$$\mathrm{MDD} = \mathrm{MDI} \cdot \mathrm{DCC} \qquad [4.2]$$

The results that follow are given in measurement time-steps that range from a few hours to seven days after intake. The data are also based off the 10-minute MDAs presented in the previous section for the collimated and uncollimated detectors and for both source geometries. As previously mentioned for $^{241}$Am, the bone surface dose, not the effective dose, will be its limiting factor. However, for comparison purposes the committed effective dose has also been calculated for $^{241}$Am. It should be noted that Tables 4.8 and 4.9 have dose values in rem whereas the other tables are in mrem.

Table 4.4: MDI and MDD for $^{60}$Co in a Male Phantom

| Days Post Intake | Fraction of Initial Intake | Minimum Detectable Intake and Committed Effective Dose | | | | | |
|---|---|---|---|---|---|---|---|
| | | Collimated (Distributed Source) | | Collimated (Point Source) | | Uncollimated | |
| | | Intake (nCi) | Dose (mrem) | Intake (nCi) | Dose (mrem) | Intake (nCi) | Dose (mrem) |
| 0.1 | 0.304 | 52.6 | 11.5 | 39.8 | 8.7 | 19.4 | 4.2 |
| 0.3 | 0.270 | 59.3 | 13.0 | 44.8 | 9.8 | 21.8 | 4.8 |
| 0.5 | 0.247 | 64.8 | 14.2 | 49.0 | 10.7 | 23.8 | 5.2 |
| 0.7 | 0.231 | 69.3 | 15.2 | 52.4 | 11.5 | 25.5 | 5.6 |
| 1.0 | 0.213 | 75.1 | 16.4 | 56.8 | 12.4 | 27.6 | 6.1 |
| 3.0 | 0.164 | 97.5 | 21.4 | 73.8 | 16.2 | 35.9 | 7.9 |
| 7.0 | 0.149 | 107 | 23.5 | 81.2 | 17.8 | 39.5 | 8.7 |
| Basis:10-minute MDA (nCi) | | 16.0 | | 12.1 | | 5.9 | |

Table 4.5: MDI and MDD for $^{131}$I in a Male Phantom

| Days Post Intake | Fraction of Initial Intake | Minimum Detectable Intake and Committed Effective Dose | | | | | |
|---|---|---|---|---|---|---|---|
| | | Collimated (Distributed Source) | | Collimated (Point Source) | | Uncollimated | |
| | | Intake (nCi) | Dose (mrem) | Intake (nCi) | Dose (mrem) | Intake (nCi) | Dose (mrem) |
| 0.1 | 0.224 | 78.5 | 2.6 | 51.8 | 1.7 | 37.4 | 1.2 |
| 0.3 | 0.175 | 100 | 3.3 | 66.3 | 2.2 | 47.9 | 1.6 |
| 0.5 | 0.137 | 128 | 4.2 | 84.7 | 2.8 | 61.2 | 2.0 |
| 0.7 | 0.106 | 166 | 5.5 | 109 | 3.6 | 79.1 | 2.6 |
| 1.0 | 0.073 | 241 | 7.9 | 159 | 5.2 | 115 | 3.8 |
| 3.0 | 0.006 | 3193 | 105 | 2106 | 69.3 | 1521 | 50.0 |
| 7.0 | 2.45E-05 | 7.18E+05 | 2.36E+04 | 4.74E+05 | 1.56E+04 | 3.42E+05 | 1.13E+04 |
| Basis:10-minute MDA (nCi) | | 17.6 | | 11.6 | | 8.4 | |

Table 4.6: MDI and MDD for $^{137}Cs$ in a Male Phantom

| Days Post Intake | Fraction of Initial Intake | Minimum Detectable Intake and Committed Effective Dose | | | | | |
|---|---|---|---|---|---|---|---|
| | | Collimated (Distributed Source) | | Collimated (Point Source) | | Uncollimated | |
| | | Intake (nCi) | Dose (mrem) | Intake (nCi) | Dose (mrem) | Intake (nCi) | Dose (mrem) |
| 0.1 | 0.226 | 141 | 4.5 | 97.1 | 3.1 | 45.9 | 1.5 |
| 0.3 | 0.179 | 177 | 5.7 | 123 | 3.9 | 57.9 | 1.8 |
| 0.5 | 0.143 | 222 | 7.1 | 154 | 4.9 | 72.5 | 2.3 |
| 0.7 | 0.113 | 281 | 9.0 | 194 | 6.2 | 91.7 | 2.9 |
| 1.0 | 0.080 | 398 | 12.7 | 275 | 8.8 | 130 | 4.1 |
| 3.0 | 0.007 | 4454 | 142 | 3079 | 98.2 | 1454 | 46.4 |
| 7.0 | 4.47E-05 | 7.10E+05 | 2.27E+04 | 4.91E+05 | 1.57E+04 | 2.32E+05 | 7.40E+03 |
| Basis:10-minute MDA (nCi) | | 31.8 | | 22.0 | | 10.4 | |

Table 4.7: MDI and MDD for $^{192}Ir$ in a Male Phantom

| Days Post Intake | Fraction of Initial Intake | Minimum Detectable Intake and Committed Effective Dose | | | | | |
|---|---|---|---|---|---|---|---|
| | | Collimated (Distributed Source) | | Collimated (Point Source) | | Uncollimated | |
| | | Intake (nCi) | Dose (mrem) | Intake (nCi) | Dose (mrem) | Intake (nCi) | Dose (mrem) |
| 0.1 | 0.304 | 36.1 | 1.0 | 23.9 | 0.7 | 15.0 | 0.4 |
| 0.3 | 0.269 | 40.8 | 1.2 | 27.0 | 0.8 | 17.0 | 0.5 |
| 0.5 | 0.246 | 44.6 | 1.3 | 29.5 | 0.8 | 18.6 | 0.5 |
| 0.7 | 0.229 | 47.9 | 1.4 | 31.7 | 0.9 | 20.0 | 0.6 |
| 1.0 | 0.211 | 52.0 | 1.5 | 34.4 | 1.0 | 21.7 | 0.6 |
| 3.0 | 0.160 | 68.6 | 1.9 | 45.4 | 1.3 | 28.6 | 0.8 |
| 7.0 | 0.140 | 78.4 | 2.2 | 51.9 | 1.5 | 32.6 | 0.9 |
| Basis:10-minute MDA (nCi) | | 11.0 | | 7.3 | | 4.6 | |

Table 4.8: MDI and MDD for $^{241}$Am in a Male Phantom, Based on CED

| Days Post Intake | Fraction of Initial Intake | Minimum Detectable Intake and Committed Effective Dose | | | | | |
|---|---|---|---|---|---|---|---|
| | | Collimated (Distributed Source) | | Collimated (Point Source) | | Uncollimated | |
| | | Intake (nCi) | Dose (rem) | Intake (nCi) | Dose (rem) | Intake (nCi) | Dose (rem) |
| 0.1 | 0.276 | 64.5 | 28.7 | 45.9 | 20.4 | 35.6 | 15.8 |
| 0.3 | 0.256 | 69.6 | 30.9 | 49.4 | 22.0 | 38.4 | 17.0 |
| 0.5 | 0.240 | 74.2 | 33.0 | 52.7 | 23.4 | 40.9 | 18.2 |
| 0.7 | 0.227 | 78.5 | 34.8 | 55.8 | 24.8 | 43.3 | 19.2 |
| 1.0 | 0.211 | 84.4 | 37.5 | 60.0 | 26.6 | 46.5 | 20.7 |
| 3.0 | 0.160 | 111 | 49.4 | 79.1 | 35.1 | 61.4 | 27.3 |
| 7.0 | 0.138 | 129 | 57.3 | 91.7 | 40.7 | 71.2 | 31.6 |
| Basis:10-minute MDA (nCi) | | 17.8 | | 12.7 | | 9.8 | |

Table 4.9: MDI and MDD for $^{241}$Am in a Male Phantom, Based on CDE

| Days Post Intake | Fraction of Initial Intake | Minimum Detectable Intake and CDE to the Bone Surface | | | | | |
|---|---|---|---|---|---|---|---|
| | | Collimated (Distributed Source) | | Collimated (Point Source) | | Uncollimated | |
| | | Intake (nCi) | Dose (rem) | Intake (nCi) | Dose (rem) | Intake (nCi) | Dose (rem) |
| 0.1 | 0.276 | 64.5 | 518 | 45.9 | 368 | 35.6 | 286 |
| 0.3 | 0.256 | 69.6 | 559 | 49.4 | 397 | 38.4 | 308 |
| 0.5 | 0.240 | 74.2 | 596 | 52.7 | 424 | 40.9 | 329 |
| 0.7 | 0.227 | 78.5 | 630 | 55.8 | 448 | 43.3 | 347 |
| 1.0 | 0.211 | 84.4 | 678 | 60.0 | 482 | 46.5 | 374 |
| 3.0 | 0.160 | 111 | 894 | 79.1 | 635 | 61.4 | 493 |
| 7.0 | 0.138 | 129 | 1036 | 91.7 | 737 | 71.2 | 571 |
| Basis:10-minute MDA (nCi) | | 17.8 | | 12.7 | | 9.8 | |

There are several results of particular interest that can be obtained from these tables. For $^{131}I$ and $^{137}Cs$, Tables 4.5 and 4.6, respectively, the lung retention fractions decrease rather rapidly from one to seven days after intake, corresponding to large increases in the MDI and MDD for these sources. In a scenario involving the inhalation of either of these radionuclides, it would be beneficial to assay people within the first twenty-four hours to increase the chance of detection.

Of even greater concern are the results for $^{241}Am$, presented in Tables 4.8 and 4.9. After two-and-a-half hours following intake, the collimated thyroid counter would only detect values that would result in a CED around 29 rem and a committed bone surface dose of approximately 520 rem. If an uncollimated probe were available, these values could be greatly reduced, as indicated in the above tables. However, these results indicate that this detection system may not be adequate to effectively assay this radioisotope and another means of detection should be analyzed.

# CHAPTER 5

# CONCLUSION

The intent of this work was to determine the feasibility of a thyroid uptake counter for monitoring lung contamination following a radiological incident that involves the public. Using MCNP5 to create various human phantom models, it was found that this detection system can be used to determine the presence of several important radionuclides in the lungs.

Minimum detectable activity limits for this detection system range from approximately 3 nCi to 0.2 μCi, depending on the characteristics of the source, detector, and the measurement environment. The committed dose corresponding to the MDA of the detection system can be determined from this information using inhalation dose conversion coefficients and intake retention fractions. The effective dose corresponding to the MDA for $^{241}$Am is rather large and depending on the dose threshold for treatment, may not be adequate to triage $^{241}$Am lung burdens of concern.

The analysis for an uncollimated detector system was performed and revealed that it was on average about eight times more efficient than a collimated system, despite the increased background count rate. In relation to measured data for the Atomlab 950, the MCNP results for a more anthropomorphic representation of the human body indicate that the capabilities of the thyroid counter can be overestimated using point sources of radiation.

In summary, this detection system can be effectively used in an RDD event to assess victims for triage, with the possible exception of an event involving $^{241}$Am. A

variety of parameters should be considered in any evaluation, such as the collimation of the detector, expected source geometry, mass of the individual, background count rate, and lung retention fractions for the radionuclide of interest.

# CHAPTER 6

# FUTURE WORK

The methods used in this work were designed to establish the feasibility of detecting inhaled contamination with a thyroid probe. However, several simplifications were made in the MCNP models that could be improved upon in future studies to better represent the effects from an RDD event. For example, despite entering the body through airways, the concentration of isotopes may have migrated to other organs and could be detected by an uncollimated detector. Metabolic modeling could be performed to obtain material distributions in the body that may influence the detector's response at various period of time after intake.

Additional analysis can be performed on the uncollimated detector geometry. Although the efficiency of the detection system is greatly improved by using an uncollimated system, the effect of a varying background counting rate has not been analyzed. It would be beneficial to establish criteria where an uncollimated detector would greatly outperform the collimated system.

MCNP modeling could also be extended to represent people of different ages, including infants, who may be contaminated in an RDD event. The use of retention factors and dose conversion coefficients applicable to these models would also be of benefit.

# APPENDIX A

# POINT SOURCE IN AIR INPUT FILE

```
C Point Source in Air with Detector System, Co-60 Case
C Cell Cards
130 10 -2.70 -13 14 imp:p=1 $Al around NaI
140 4 -3.67 -14 imp:p=1 $NaI detector
150 5 -11.35 -15 13 16 19 imp:p=1 $Lead 1
160 3 -0.00129 -16 -15 13 19 imp:p=1 $Air cone
190 3 -0.00129 -19 13 imp:p=1 $Air behind NaI
998 3 -0.00129 15 -99 imp:p=1 $Air in system
999 0 99 imp:p=0 $Outside Universe

C Surface Cards
13 rcc 15.24 0 0 5.18 0 0 2.59 $Al around NaI
14 rcc 15.29 0 0 5.08 0 0 2.54 $NaI detector
15 rcc 0 0 0 27.99 0 0 4.65175 $Lead collimator and housing
16 k/x 33.997 0 0 0.0183378 -1 $Collimator hole
19 rcc 20.37 0 0 7.62 0 0 2.54 $Gap behind NaI
99 rpp -500 500 -100 100 -100 100 $Universe Box

C Data Cards
C Material Cards
m3 7014 .755267 8016 .231781 6000 .000125 18000 .012827 $Air
m4 11000 .5 53000 .5 $NaI
m5 82000 1 $Lead
m10 13000 1 $Aluminum
C Source Definition
sdef pos=-50 0 0 erg=d1 par=2
si1 l 1.17 1.33 $Co-60
sp1 0.9986 0.9998
f8:p 140
f18:p 140
ft18 GEB -0.0060465 0.06261 0.015694
e18 0 1024i 2.5
e8 0 .997 1.533 2 2.5 $Co-60
mode p
print
nps 1E7
```

# APPENDIX B

# SLAB PHANTOM INPUT FILE

```
C Acrylic Slab Phantom and Detector System, Ir-192 Case
C Cell Cards
100 1 -1.19 -10 11 imp:p=1 $Source Slab
110 3 -0.001293 -11 imp:p=1 $Air Space in Slab
120 1 -1.19 -12 imp:p=1 $Other Slabs
130 10 -2.70 -13 14 imp:p=1 $Al around NaI
140 4 -3.67 -14 imp:p=1 $NaI detector
150 5 -11.35 -15 13 16 19 imp:p=1 $Lead 1
160 3 -0.001293 -16 -15 13 19 imp:p=1 $Air cone
190 3 -0.001293 -19 13 imp:p=1 $Air behind NaI
998 3 -0.001293 15 10 12 -99 imp:p=1 $Air in system
999 0 99 imp:p=0 $Outside Universe

C Surface Cards
10 rpp -26.191 -23.81 -14.9225 14.9225 -14.9225 14.9225 $Slab with Source
11 rcc -24.762 0 0 .952 0 0 1.42875 $Air space in slab
12 rpp -23.81 0 -14.9225 14.9225 -14.9225 14.9225 $Other Slabs
13 rcc 15.24 0 0 5.18 0 0 2.59 $Al around NaI
14 rcc 15.29 0 0 5.08 0 0 2.54 $NaI detector
15 rcc 0 0 0 27.99 0 0 4.65175 $Lead collimator and housing
16 k/x 33.997 0 0 0.0183378 -1 $Collimator hole
19 rcc 20.37 0 0 7.62 0 0 2.54 $Gap behind NaI
99 rpp -500 500 -100 100 -100 100 $Universe Box

C Data Cards
C Material Cards
m1 6000 .3333 8016 .1333 1001 .5334 $Lucite
m3 7014 .755267 8016 .231781 6000 .000125 18000 .012827 $Air
m4 11000 .5 53000 .5 $NaI
m5 82000 1 $Lead
m10 13000 1 $Aluminum
C Source Definition
sdef pos=-24.06 0 0 erg=d1 par=2
si1 l .296 .308 .317 .468 .485 .589 .604 .612 $Ir-192
sp1 .290 .297 .828 .478 .0316 .0452 .0818 .0533
f8:p 140
f18:p 140
ft18 GEB -0.0060465 0.06261 0.015694
e18 0 1024i 2.5
e8 0 .250 .703 1 2.5 $ Ir-192
mode p
nps 5E7
```

# APPENDIX C

# WATER-FILLED PHANTOM INPUT FILE

```
C Water-Filled Phantom and Detector System, ~100cm Case
C Cell Cards
1 1 -1.19 -1 imp:p=1
2 1 -1.19 -2 imp:p=1
3 1 -1.19 -3 imp:p=1
4 1 -1.19 -4 imp:p=1
5 1 -1.19 -5 imp:p=1
6 1 -1.19 -6 imp:p=1
7 6 -1 -7 imp:p=1 $Water in system
130 10 -2.70 -13 14 imp:p=1 $Al around NaI
140 4 -3.67 -14 imp:p=1 $NaI detector
150 5 -11.35 -15 13 16 19 imp:p=1 $Lead 1
160 3 -0.00129 -16 -15 13 19 imp:p=1 $Air cone
190 3 -0.00129 -19 13 imp:p=1 $Air behind NaI
998 3 -0.00129 1 2 3 4 5 6 7 15 -99 imp:p=1 $Air in system
999 0 99 imp:p=0 $Outside Universe

C Surface Cards
1  rpp -16 0 -11.75 11.75 14.8 15 $Top of Container
2  rpp -16 0 -11.75 11.75 -15 -14.8 $Bottom of Container
3  rpp -16 0 -11.75 -11.55 -14.8 14.8 $Narrow side 1
4  rpp -16 0 11.55 11.75 -14.8 14.8 $Narrow side 2
5  rpp -0.2 0 -11.55 11.55 -14.8 14.8 $Front broad
6  rpp -16 -15.8 -11.55 11.55 -14.8 14.8 $Rear broad
7  rpp -15.8 -0.2 -11.55 11.55 -14.8 13.2 $Water
13 rcc 105.24 0 -.8 5.18 0 0 2.59 $Al around NaI
14 rcc 105.29 0 -.8 5.08 0 0 2.54 $NaI detector
15 rcc 90 0 -.8 27.99 0 0 4.65175 $Lead collimator and housing
16 k/x 123.997 0 -.8 0.0183378 -1 $Collimator hole
19 rcc 110.37 0 -.8 7.62 0 0 2.54 $Gap behind NaI
99 rpp -500 500 -100 100 -100 100 $Universe Box

C Data Cards
C Material Cards
m1 6000 .3333 8016 .1333 1001 .5334 $Lucite
m3 7014 .755267 8016 .231781 6000 .000125 18000 .012827 $Air
m4 11000 .5 53000 .5 $NaI
m5 82000 1 $Lead
m6 1000 .6666 8016 .3334 $Water
m10 13000 1 $Aluminum
C Source Definition
sdef erg=d1 x=d2 y=d3 z=d4 par=2 cel=7
si1 l .3645 .637 $I-131
sp1 0.812 0.0727
si2 -15.8 -0.2
sp2 0 1
```

```
si3 -11.55 11.55
sp3 0 1
si4 -14.8 13.2
sp4 0 1
f8:p 140
f18:p 140
ft18 GEB -0.0060465 0.06261 0.015694
e18 0 1024i 2.5
e8 0 .309 .420 1 2.5
mode p
print
nps 5E7
```

# APPENDIX D

# HUMAN PHANTOM INPUT FILE (CONDENSED)

```
C Male Phantom at  21.0 Years
C Since this input file is licensed for the user only, only the headings that describe the
C body parts and organs that were included in the model have been included in this
C Appendix.  The detector geometry and source definitions that were combined with this
C input deck are also included.
c +++++++++++++++++++++++++++++++++++++++++
c   File Prepared by Body Builder
c   CopyRight 1996-2004, White Rock Science
c   This input file is for the use of
c   BodyBuilder License holder only.
c   Distribution is Prohibited.
c +++++++++++++++++++++++++++++++++++++++++
c +++++++++++++++++++++++++++++++++++++++++++++++
c         CELLS
c +++++++++++++++++++++++++++++++++++++++++++++++
c       LEG BONES
c       ARM BONES
c       PELVIS
c       SPINE
c       SKULL & FACE
c       RIBS
c       CLAVICLES
c       SCAPULAE
c       ADRENALS
c       BRAIN
c       GALL BLADDER
c       ESOPHAGUS
c       STOMACH
c       SMALL INTESTINE
c       ASCENDING COLON
c       TRANSVERSE COLON
c       DESCENDING COLON
c       SIGMOID COLON
c       HEART
c       KIDNEYS
c       LIVER
c       LUNGS
c       PANCREAS
c       SPLEEN
c       TESTICLES
c       THYMUS
c       THYROID
c       URINARY BLADDER
c       PENIS & SCROTUM
c       SKIN
c         Trunk Skin
```

```
c        Penis & Scrotum Skin
c       Legs Skin
c          HEAD
c          NECK
c       OUTER TRUNK---ARMS & SCAPULAE
c       UPPER TRUNK---ABOVE RIBS
c       UPPER RIB CAGE
c       LOWER RIB CAGE
c       HIGH CHEST ORGANS
c       CHEST---LIVER LEVEL
c       LOWER TRUNK
c       LEGS
c       SURROUNDING AIR
c          air          OUTSIDE of NECK
c
c  Detector setup
602 5 -3.67 -800 imp:p=1 $NaI detector
603 6 -11.35 -801 804 802 805 imp:p=1 $Lead 1
604 4 -0.001293 -801 -802 800 804 805 imp:p=1 $Air cone
605 10 -2.70 -804 800 imp:p=1 $Al around NaI
608 4 -0.001293 -805 804 imp:p=1 $Air behind NaI
c       VOID
700   0             600
          imp:p =0

c +++++++++++++++++++++++++++++++++++++++++++++++++
c         SURFACES
c +++++++++++++++++++++++++++++++++++++++++++++++++
.
.
.

c +++++++++++++++++++++++++++++++++++++++++++++++++
c
c       TRANSFORMATIONS
c +++++++++++++++++++++++++++++++++++++++++++++++++
.
.
.
c +++++++++++++++++++++++++++++++++++++++++++++++++
c     MATERIALS
c +++++++++++++++++++++++++++++++++++++++++++++++++
.
.
.
m5 11000 .5 53000 .5 $NaI
```

```
m6 82000 1 $Lead
m10 13000 1 $Aluminum
C Source Definition
sdef erg=d1 x=d2 y=d3 z=d4 par=2 cel=330
c si1 l 1.17 1.33 $Co-60
c sp1 0.9986 0.9998
C si1 l 0.6617 $Cs-137
C sp1 0.851
C si1 l 0.0595 $Am-241
C sp1 0.359
C si1 l .3645 .637 $I-131
C sp1 0.812 0.0727
si1 l .296 .308 .317 .468 .485 .589 .604 .612 $Ir-192
sp1 .290 .297 .828 .478 .0316 .0452 .0818 .0533
si2 -13.7 13.7
sp2 0 1
si3 -7.6 7.6
sp3 0 1
si4 43.4 67.6
sp4 0 1
f8:p 602
f18:p 602
ft18 GEB -0.0060465 0.06261 0.015694
C f28:p 140
C e28 0 .040 .073 1 2.5 $Am-241
C e8 0 .015 .075 1 2.5
e18 0 1024i 2.5
c e8 0 .997 1.533 2 2.5 $Co-60
C e8 0 .561 .761 1 2.5 $ Cs-137
e8 0 .250 .703 1 2.5 $ Ir-192
C e8 0 .328 .400 1 2.5 $ I-131
mode p
print
nps 1E8
```

## REFERENCES


Anigstein, R., Erdman, M.C., King, S.H., Mauro, J.J., Miller, K.L. (2005). An Evaluation of Hospital Radiation Detectors for Use in Screening Potentially Contaminated Individuals. Review Draft Prepared for Centers for Disease Control and Prevention.

Arqueros, F. and Montesinos, G.D. (2003). A Simple Algorithm for the Transport of Gamma Rays in a Medium. American Journal of Physics, Volume 71, No. 1.

Autret, D., et al. (2005). Monte Carlo Modeling of Gamma Cameras for I-131 Imaging in Targeted Radiotherapy. Cancer Biotherapy and Radiopharmaceuticals, Volume 20, No. 1.

Currie, L.A. (1968). Limits for Qualitative Detection and Quantitative Determination: Application to Radiochemistry. Analytical Chemistry, Volume 40, No. 3.

Erdman, M.C. (2005). Personal Communication. Friday, July 1.

Ferguson, C.D. (2003). Reducing the threat of RDDs. IAEA Bulletin 45/1.

Flinn, F.B. (1929). Some Precautions to be Taken When Making Tests for Radioactivity in the Living Body. American Journal of Roentgenology and Radium Therapy, Volume 22.

Franck, D., et al. (2003). Application of Monte Carlo Calculations to Calibration of Anthropomorphic Phantoms Used for Activity Assessment of Actinides in Lungs. Radiation Protection Dosimetry, Volume 105, No. 1-4.

Hickman, D.P. (1994). In Vivo Measurements. Internal Radiation Dosimetry Health Physics Society Summer School. (Medical Physics Publishing, Madison,WI)

Jarret, Col. D.G. et al. (2003). Medical Management of Radiological Casualties Handbook, Second Edition. AFRRI Special Publication 03-1.

Keenan, A. (1999). First Observations of Excited States in the Neutron Deficient Nuclei $^{160,161}$W and $^{159}$Ta. PhD Thesis, University of Liverpool.

Knoll, G.F. (2000). Radiation Detection and Measurement, Third Edition. (John Wiley and Sons, New York).

Kramer, G.H., Crowley, P., Burns, L.C. (2000). Investigating the Impossible: Monte Carlo Simulations. Radiation Protection Dosimetry, Volume 89, No. 3-4.

Kramer, G.H., Burns, L.C., Guerriere, S. (2002). Monte Carlo Simulation of a Scanning Whole Body Counter and the Effect of BOMAB Phantom Size on the Calibration. Health Physics, Volume 83, No. 4.

Lessard, E.T., et al. (1987). Interpretation of Bioassay Measurements. NUREG/CR-4884, U.S. Nuclear Regulatory Commission, Washington, D.C.

Lugar, Sen. Richard G. (2005). The Lugar Survey on Proliferation Threats and Responses. http://lugar.senate.gov/reports/NPSurvey.pdf (Accessed August 8, 2005).

National Council on Radiation Protection (NCRP) (1980). Management of Persons Accidentally Contaminated with Radionuclides, NCRP Report 65. Washington, D.C.: NCRP.

Oliveira, C.A.N., Lourenço, M.C., Danta, B.M., Lucena, E.A. (1991). Design and Operation of a Whole-Body Monitoring System for the Goiânia Radiation Accident. Health Physics, Volume 60, No. 1.

Pacific Northwest National Lab (PNNL) (2003). Radiation and Health Technology: Methods and Models of the Hanford Internal Dosimetry Program. PNNL-MA-860, Richland, WA.

Schlundt, H., Baker, H.H., Flinn, F.B. (1929). The Detection and Estimation of Radium and Mesothorium in Living Persons I. American Journal of Roentgenology and Radium Therapy, Volume 21.

Stansbury, P.S. (1994). An Overview of Monte Carlo Techniques Used in Internal Dose Calculations and Their Statistical Interpretation. Internal Radiation Dosimetry Health Physics Society Summer School. (Medical Physics Publishing, Madison,WI)

Steinmeyer, P., Jr. (1998). Detection Sensitivity and MDA (Part 1). Ludlum Report, Volume 13, No. 1.

Taylor, G.A. (2000). The Evolution of Internal Dosimetry Bioassay Methods at the Savannah River Site. Savannah River Company Report. WSRC-MS-2000-00290.

Toohey, R. et al. (1991). Current Status of Whole-Body Counting as a Means to Detect and Quantify Previous Exposures to Radioactive Materials. Health Physics, Volume 60, Sup. 1.

U.S. Environmental Protection Agency (EPA) (1988). Limiting Values of Radionuclide Intake and Air Concentration and Dose Conversion Factors for Inhalation, Submersion, and Ingestion. Federal Guidance Report No. 11, EPA-520/1-88-020, Washington, D.C.

Van Riper, K.A. (2004). White Rock Science Tools for Geometry Modeling. Transactions of the American Nuclear Society, Volume 91.

White Rock Science (2004). BodyBuilder, www.whiterockscience.com/wrs.html (Accessed May 18, 2005).